Tampere University

Hassan Junaid

SIMULATION, FABRICATION AND CHARACTERIZATION OF 940nm GaAs-based EDGE EMITTING LASER EPITAXIAL STRUCTURES

Master's Thesis
Faculty of Engineering and Natural Sciences
Examiner: D.Sc. Jukka Viheriälä
D.Sc. Heidi Tuorila
December 2025

ABSTRACT

Junaid Hassan: Simulation, fabrication and characterization of 940nm GaAs-based edge emitting laser epitaxial structures
Master's thesis
Tampere University
Science and Technology
December 2025

Single- and few-photon generation based on III–V semiconductor platforms is becoming central to advanced quantum communication and quantum key-distribution (QKD) systems, where compact, energy-efficient, and wavelength-stable light sources are essential. State-of-the-art quantum photonic experiments still rely heavily on Ti:sapphire excitation at 900-1000 nm; however, the large footprint, cost, and limited integrability of these systems restrict their practical implementation in scalable quantum networks. III–V semiconductor monolithic and integrated mode-locked laser diodes (MLLDs) offer a highly promising alternative due to their compact form factor, low power consumption, and compatibility with photonic integration roadmaps. InGaAs/AlGaAs heterostructures naturally support emission in the 900-1200 nm band, making them suitable candidates for quantum-photonics-grade sources around 940 nm.

Prior to the development of MLLDs, it is imperative to verify and quantify the optical gain, material quality, and carrier transport characteristics of the epitaxial wafers grown using molecular beam epitaxy (MBE). This thesis systematically investigates the performance of in-house grown GaAs-based epitaxial structures engineered for emission near 940 nm. Edge-emitting ridge-waveguide lasers were fabricated to experimentally assess the epitaxial quality and device-level gain performance. A comprehensive characterization was carried out, including I-L-V measurements, extraction of external differential quantum efficiency, estimation of internal quantum efficiency and internal optical losses, evaluation of characteristic temperature, far-field divergence, and spectral behavior under different injection conditions.

In parallel with the experimental work, detailed device-level optical and electronic simulations were performed to validate the epitaxial design. Band-structure simulations were used to examine carrier confinement, and changes in the band profile under forward-bias injection. Furthermore, the simulated I-L-V characteristics and distributed loss mechanisms, including free-carrier absorption, intervalence-band absorption, and thermally induced leakage, were analyzed to correlate with the measured device performance. The combined simulation-experiment approach provides a robust assessment of the wafer quality and establishes a reliable foundation for the future development of monolithically and integrated MLLDs for quantum-communication applications.

Keywords: Quantum key distribution (QKD), Molecular beam epitaxy (MBE), Mode locked laser diode (MLLD), InGaAs/AlGaAs heterostructures, I-L-V characteristics, Loss mechanisms.

USE OF AI IN THESIS

I have utilised AI tools in my thesis:

☐ No

☒ Yes

The AI tools utilised in my thesis, and their purposes are described below:

Names and versions of AI tools: ChatGPT-5.1 model, QuillBot 10.2 version 4.44.0

Purpose of using AI tools: I mainly used AI in my thesis work to improve writing style and rephrase words for better grammatical understanding in a way that it aligns with my research work.

Sections where AI tools were used: I used ChatGPT particularly to explore and understand academic research papers and QuillBot for identifying and rectifying grammatical errors.

I acknowledge that I am fully responsible for the entire content of my thesis, including the parts generated by AI, and accept accountability for any violations of ethical standards in publications.

PREFACE

My master's thesis was carried out at the Optoelectronics Research Centre (ORC), Tampere University. I am very thankful to my thesis supervisor, Dr. Jukka Viheriälä, for all his scientific knowledge, patience, and constant help throughout this work. I would also like to express my sincere appreciation to Dr. Mircea Gunia, group leader at ORC, for his invaluable support and encouragement, and for providing an environment that enabled both professional growth and meaningful learning.

My heartfelt thanks go to my co-supervisor D.Sc. Heidi Tuorila for her continuous support, practical advice, and encouragement during this thesis process. I am also thankful to the entire ORC team for creating such a motivating and friendly research atmosphere. The discussions in the lab, the collaborative spirit, and the memorable moments shared with colleagues have significantly enriched my experience.

I extend my appreciation to the cleanroom team especially to Mervi Koskinen, Helmer Piirilä and Behzad Namvar for their guidance, training, and for trusting me with responsibilities that strengthened my skills in semiconductor device fabrication. Their expertise and willingness to help have played an essential role in my development.

My sincere gratitude to Numan Zia, who has always been my mentor. His dedication to the field and his insightful perspective on semiconductor physics and photonics have continuously inspired me to refine my own understanding and professional practice. My scientific career growth has been significantly shaped by his support.

Lastly, I want to express my gratitude to my friends and fellow students for the support and companionship that made this journey enjoyable. And most importantly my family, especially my sisters, for their unwavering encouragement throughout my life.

Tampere, 16th December 2025

Junaid Hassan

TABLE OF CONTENT

LIST OF FIGURES

LIST OF SYMBOLS AND ABBREVIATIONS

Al	Aluminum
AlGaAs	Aluminum gallium arsenide
AlN	Aluminum nitride
AR	Anti reflection coating
CW	Continuous wave
DH	Double heterostructure
EEL	Edge emitting laser
GaAs	Gallium arsenide
HMDS	Hexamethyldisilazane
HR	High reflection coating
ILV	Current-Light-Voltage characteristics
InGaAs	Indium gallium arsenide
InP	Indium phosphide
LD	Laser diode
MBE	Molecular beam epitaxy
MLLD	Mode locked laser diode
PIC	Photonic integrated circuit
PECVD	Plasma enhanced chemical Vapor deposition
QKD	Quantum key distribution
QW	Quantum well
RTA	Rapid thermal annealing
SEM	Scanning electron microscope
SiC	Silicon carbide
SiO2	Silicon dioxide
SRH	Shockley-Read-Hall recombination
T_0	Characteristic temperature
VCSEL	Vertical cavity surface emitting laser
h	Planck's constant
ν	Frequency of photon
E_{1hh} , E_{2hh} , E_{3hh}	Confined energy levels for electrons
E_{1lh} , E_{2lh}	Confined energy levels for holes
k	Boltzmann constant
α_i	Internal losses
η_i	Internal quantum efficiency

η_d	Differential quantum efficiency
τ	Carrier lifetime
τ_p	Photon lifetime
β_{sp}	Spontaneous emission coupling factor
n_1	Cladding refractive index
n_2	Active region refractive index
n_e	effective refractive index
R_s	Series Resistance
I_{th}	Threshold current
J_{th}	Threshold current density
λ	Wavelength

1. Introduction

Photonics integration has become a key enabler to drive the advancement in telecommunication [1], defense [2], biosensing [3] and quantum communication [4]. Photonics integrated circuits (PICs), originally deployed for optical communication systems, are now revolutionizing quantum technology [5] by shrinking bulky and costly systems onto compact chips, enabling scalable, low-cost, and practical quantum secure communication. Figure 1.1 shows different photonics integration material platforms, the key integrated photonics components and common quantum communication applications. In terms of material, the most common platforms are based on silicon and indium phosphide. The main quantum photonic components include photodetectors [6], high-speed modulators [7] and quantum light sources [8], and common applications are quantum teleportation [9] and quantum key distribution (QKD) [10]. Single-photon light source [11], emitting in the 900-1000 nm range, is the key enabling part of a QKD system [12]. Currently, pulsed Ti:Sapphire lasers are commonly used as pump sources for single photon generation [13], which are bulky, costly and hard to scale. To this end, pulsed semiconductor light sources such as mode-locked laser diodes (MLLD) [14] are the best alternative as the optical pump sources for single-photon generation in this wavelength range due to their small footprint, power efficiency and cost effectiveness. Semiconductor lasers emitting around 940 nm [15] have been developed for a variety of applications such as optical pumping of solid-state lasers, fiber amplifiers and medical treatment [16]. InGaAs/AlGaAs quantum well heterostructures can emit light between 900nm – 1200nm [17], where high power emission around 940 nm has been reported in different studies [18]. However, less focus has been given to the development of mode-locked lasers emitting in 940 nm range, which are suitable as pump sources for single-photon emission.

In this work we design, fabricate and characterize InGaAs/AlGaAs stripe oxide lasers emitting around 940 nm to validate the performance of epitaxial material for mode-locked lasers developments. This thesis comprises a comprehensive study including theoretical analysis, simulations of epitaxial structure, fabrication, and electro-optical characterization. The results give a pretty good agreement between the simulation results and the actual values of key parameters like current-light-voltage (ILV)

characteristics of fabricated devices giving a base for next step of MLLD development from these epitaxial structures.

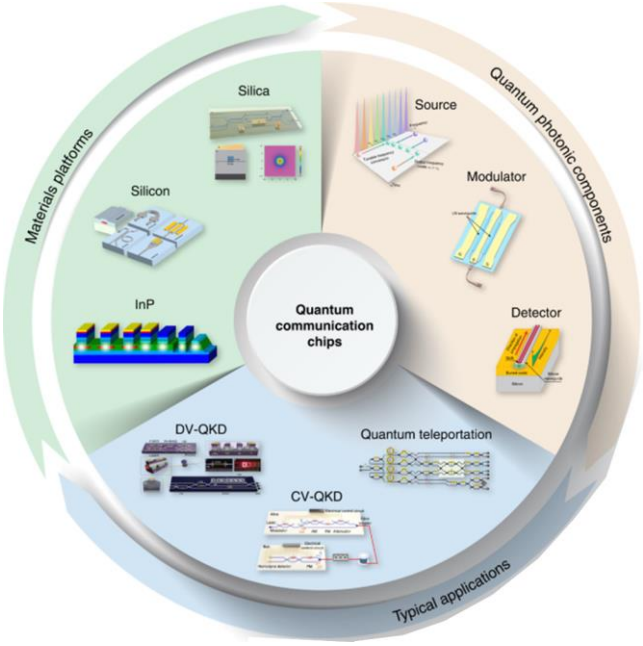

Figure 1.1 Material platform for photonics integrated circuits and their applications in quantum communication.

1.1. Structure of thesis

This thesis is organized in the following way in terms chapters:

Chapter 1 gives a quick overview of the thesis's main subject and the motivations behind this study.

Chapter 2 provides the theoretical framework, discussing the fundamental physics of semiconductor lasers and the III–V material systems relevant to this study.

Chapter 3 introduces edge-emitting lasers, focusing on their optical mode confinement and far-field emission characteristics.

Chapter 4 addresses the design and simulation of 940 nm GaAs epitaxial structures using the HAROLD software, followed by a detailed description of their molecular beam epitaxy (MBE) growth and subsequent device fabrication processes.

Chapter 5 gives the experimental characterization of the fabricated 940 nm GaAs edge-emitting lasers is presented, where critical performance metrics, including LIV characteristics, threshold current, internal and external quantum efficiencies, internal

optical losses, characteristic temperature, and lasing wavelength are systematically analyzed.

Finally, **Chapter 6** summarizes the key outcomes of this work and outlines perspectives for future advancements in GaAs-based near-infrared edge-emitting laser technologies.

2. Theoretical background

In this chapter, fundamental principles of semiconductor physics and laser theory are discussed. Recombination mechanisms in semiconductor materials are generally divided into two types: First is radiative recombination and the second is non-radiative recombination. When the electron from the conduction band transitions in the valance band to a vacant state (hole), accompanied by emission of a photon, this combination is referred to as radiative recombination. In modern semiconductor lasers, the important radiative transitions are i) radiative absorption, ii) spontaneous emission, and iii) stimulated emission. In stimulated emission, the incident and the released photons are identical in terms of momentum and energy, which is the fundamental principle of laser operation. Nonradiative recombination, by contrast, occurs without photon emission and is significantly influenced by parameters such as temperature, and carrier concentration.

The semiconductor laser is commonly realized by an electrically pumped forward biased p–n junction structure, wherein optical gain can be achieved by injecting carriers into a thin active region commonly names as quantum well. The optical feedback can be provided by as-cleaved facets of the semiconductor crystal, functioning as partially reflecting mirrors. When the injected current density reaches a threshold current density J_{th} at which gain is sufficient to compensate for the cavity losses, the lasing threshold is reached. Beyond this threshold, additional carrier injection results in photon generation through stimulated emission. Although lasers have many similarities, a semiconductor laser operates independently from other laser types.

In Section 2.1, the fundamental recombination mechanisms in semiconductor materials are introduced. This includes a discussion of radiative recombination processes, which form the basis of light generation in lasers, and nonradiative mechanisms, which represent key loss channels. Section 2.2 addresses the effect of temperature on device performance. Carrier leakage across heterobarriers, and the injected current's temperature dependency are all given particular focus. Section 2.3 introduces the Fabry-Perot cavity diode laser as a representative structure for understanding semiconductor laser operation. The analysis emphasizes essential principles such as output power threshold current, internal and external quantum efficiencies and optical losses in the cavity. Section 2.4 discusses GaAs-based material systems, focusing on lattice structure, the role of defects, and the effects of strain in quantum well layers. Finally, the specific epitaxial material structures employed in this thesis are presented.

2.1. Recombination mechanisms

This section discusses the two major carrier recombination processes governing the performance of semiconductor lasers, namely radiative and non-radiative recombinations.

2.1.1. Radiative recombination

In semiconductors, electrons occupy specific energy states which can be determined by quantum physics and Schrodinger's equation [19]. At absolute zero (0K), semiconductor materials exhibit a band structure analogous to that of insulators, consisting of an unoccupied conduction band and a maximum filled valence band, which are separated by a band gap significantly smaller (typically < 3eV) containing no allowed energy states [20].

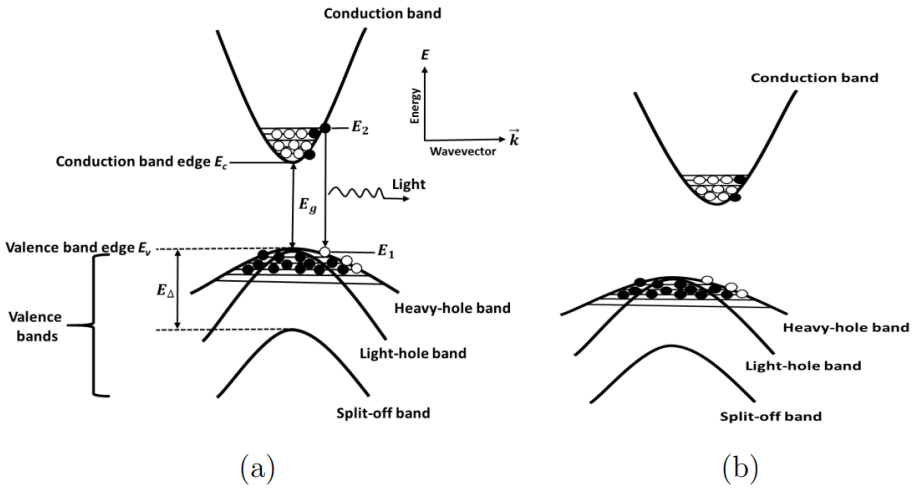

Figure 2.1 Energy-wave-vector (E-k) schematic showing a single conduction band alongside the split-off, light-hole and heavy-hole valance bands.

Valence band (E_v) is situated below the bandgap, while the conduction band (E_c) is positioned above it, with both bands encompassing energy levels for holes and electrons The valence band has three sub-bands: split-off (SO), light hole (LH) and heavy hole (HH valence bands as shown in Figure 2.1.

In this figure, E_g is bandgap energy, defined as the difference of the energies between maximum of the valence band and the minimum of the conduction band. At room temperature, the band gap values for III-V semiconductors vary from 0.18 eV for indium antimonide to 3.4 eV for GaN [20]. As a function of the crystal momentum (k-vector), the

figure also depicts the semiconductor band structure related to the electrons within the crystal lattice. The two types of bandgaps can be characterized by the values of the k-vector Figure 2.1 (a) illustrates that the valance and conduction bands exhibit their maximum and minimum points at an identical k-vector value, which is referred to as a direct bandgap . In Figure 2.1 (b), the k-vector values are different for maximum and minimum of the valence and conduction bands, indicating an indirect bandgap. Intrinsic semiconductors, like germanium (Ge) and silicon (Si), exhibit an indirect bandgap, which constrains their efficacy in optoelectronic applications owing to inadequate radiative recombination. Conversely, indium phosphide (InP), gallium arsenide (GaAs), and gallium antimonide (GaSb), demonstrate a straight bandgap, facilitating effective light emission.

In a semiconductor, the maximum occupied energy level at zero kelvin temperature is called Fermi energy E_f. At this temperature, all energy states below E_f are filled with electrons, while those above are empty.

When additional holes and electrons are introduced into the semiconductor, for example, by doping or excitation, the system is no longer in a state of equilibrium. In such cases, the distribution of holes and electrons is better described using separate energy levels known as quasi-Fermi levels, i.e., in the conduction band E_{fc} for electrons and in the valence band E_{fv} for holes. These quasi-Fermi levels indicate the effective energy levels that govern the occupation of states by electrons and holes under non-equilibrium conditions. Additionally, Figure 2.1 (a) E_Δ represents the difference of energy between the maximum of spin-orbit (SO) split-off band and the maximum of the valence band. The significance of E_Δ will be addressed in section 2.1.2 for the case of nonradiative recombination.

Absorption of light

In direct-band-gap semiconductors, like GaAs, InP, or GaSb, a photon with energy over the bandgap has a high chance of being absorbed in thermal equilibrium. The electron in the valence band absorbs the energy emitted by the photon, thereby transitioning to the conduction band. In this process, the photon's energy $E=h\nu$ must be at greater than or equal to the bandgap energy E_g. The energy enables an electron to transition from a lower energy state in the valence band (denoted as E_1) to a higher energy state in the conduction band (denoted as E_2), as shown in Figure 2.2 (a).

However, if the energy of the photon is less than the bandgap, it will not be absorbed. This means that semiconductors with large bandgaps are transparent to low-energy

electromagnetic radiation, as such photons lack the energy required to promote electrons across the bandgap.

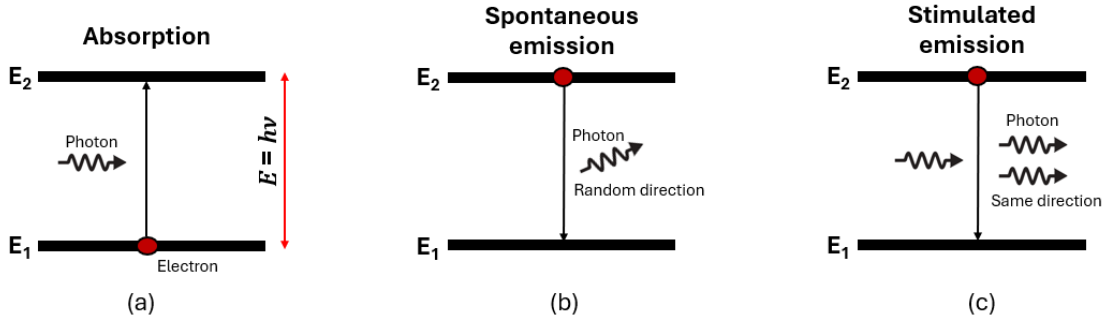

Figure 2.2 Interband radiative transitions. a) Incident photon absorption, b) spontaneous emission c) stimulated emission showing the incident and released photons are identical.

Optical gain

Stimulated emission is the fundamental principle underlying laser operation. In this process, an incident photon interacts with the conduction band's electron, causing the electron to transition to state in the valence band with low energy. As a result, a second photon is emitted that is identical to the incident photon in terms of frequency, energy, phase, and direction of propagation. This coherent emission process is illustrated in Figure 2.2 (c) and is central to the functioning of semiconductor lasers [21], [22].

The semiconductor must reach a state known as population inversion, where the density of electrons in the conduction band is greater than the hole density in the valence band, for stimulated emission to dominate over absorption. Under these non-equilibrium conditions, the optical intensity within the material increases exponentially due to repeated stimulated emissions. When the rate of stimulated emission becomes greater than the rate of absorption, the semiconductor exhibits a net optical gain (g). This gain enables the amplification of light, which is essential for laser generation.

Carrier density and thermal effects on optical gain

In an active region, the presence of high concentrations of electrons and holes gives rise to many-body interactions, which significantly influence optical properties. These interactions, prominent at higher carrier densities, lead to bandgap renormalization, often referred to as bandgap shrinkage [21]. As a result, the optical gain spectrum undergoes

a redshift, meaning the peak gain moves toward longer wavelengths. Furthermore, a distortion in the spectral form is also present along with this redshift.

Initially, the bandgap shrinkage dominates the spectral behavior, but as the carrier density continues to increase, the influence of this effect diminishes. This is due to the spatial spreading of carrier wavefunctions, which reduces their interaction strength and limits further shrinkage [23].

At even higher carrier densities, band-filling effects become significant. Electrons and holes begin to occupy higher energy subbands, resulting in emission wavelength to shift toward the shorter wavelength (higher energy) side. This effect, also known as the Burstein-Moss shift, leads to a blue shift in the gain spectrum and a broadening of the spectral profile [24]. Ultimately, the blue shift induced by band-filling can surpass the redshift caused by bandgap shrinkage, especially at very high carrier densities.

Temperature also significantly influences the gain characteristics. At elevated temperatures, thermal broadening of the carrier distribution occurs due to increased kinetic energy. This broadening spreads carriers over a wider range of energy states in the conduction and valance bands, as governed by the Fermi-Dirac distribution. Consequently, a higher injected carrier density is required to achieve the same level of population inversion and optical gain.

In summary, the gain spectrum of a semiconductor laser is the result of a complex interplay between carrier-induced effects and thermal influences. At low carrier densities, bandgap shrinkage dominates, leading to redshift, whereas at high densities, band-filling leads to blueshift. Simultaneously, temperature increases demand higher injection levels to maintain performance due to carrier redistribution.

Spontaneous and amplified spontaneous emission

The most fundamental radiative recombination process in semiconductors is spontaneous emission. In this process, an electron in the conduction band jumps to the valence band, emitting a photon as shown in Figure 2.2 (b). This emission occurs spontaneously, without external stimulation, and the emitted photon has a random direction, polarization and phase, making the radiation inherently incoherent. The rate of spontaneous emission depends on the carrier population and can be enhanced by external pumping. Pumping can introduce additional electrons and holes into the material either by optical means (through photons with energies exceeding the bandgap energy) or through current injections, where carriers are supplied directly via current. Increasing the carrier density through such methods raises the likelihood of spontaneous recombination, thereby enhancing the spontaneous emission output.

The amplified spontaneous emission (ASE) is the spontaneous emission which is a representation of the radiation that the semiconductor emits in free space. The concentration of carriers has a direct impact on the positioning of the spontaneous emission spectrum.

Temperature also has a significant impact in modulating the emission spectrum. Fermi distribution is broadened by self-heating and recombination heat, increasing the higher-energy states occupation probability, which leads to a blue shift in the emission spectrum due to band-filling effects. In addition, temperature-induced bandgap narrowing may cause emission spectrum to have a red shift [25]. The amplified spontaneous emission spectrum is derived from both the optical gain spectra and spontaneous emission [25]. Like spontaneous emission, the ASE spectrum is influenced by band-filling, bandgap narrowing, and self-heating, all of which contribute to shifts in its spectral characteristics.

Quantum well (active region)

In bulk semiconductors, conduction band electrons can move freely in three-dimensional lattice and have a continuous density of states for electrons within the conduction and valence bands. However, this unrestricted carrier motion limits control over optical transition rates. To overcome this, semiconductor heterostructures incorporating quantum wells (QWs) are employed. A quantum well is formed by placing thin layer of lower bandgap material between layers of higher bandgap materials, creating a potential well that confines carriers in one dimension.

This confinement results in quantized energy levels, enhancing the probability of radiative recombination and improving the efficiency of light absorption and emission in devices such as laser diodes. The thickness of a quantum well (QW) is usually between 5 and 20 nm. It is made up of a material with a narrower bandgap enclosed between two materials with wider bandgaps. The electrons and holes can be confined inside a very thin layer of QW by means of barriers.

Figure 2.3 shows the energy levels of holes and electrons confined within a quantum well. For heavy holes these confined energy levels are denoted by E_{1hh}, E_{2hh}, and E_{3hh}, and for light holes E_{1lh} and E_{2lh}, while for electrons by E_{1c}, E_{2c}, and E_{3c}. E_g is QW energy bandgap, ΔE_c and ΔE_v are conduction and valance band energies respectively.

In the quantization of energy state, the ground level is even raised to a higher energy value, it is evident that the transition energy $h\nu$ associated with electron-hole pair recombination is greater than the bandgap energy E_g. In comparison to bulk materials, the energy level quantization gives narrower emission spectra. A quantum well structure gives more gain a than bulk active region [21].

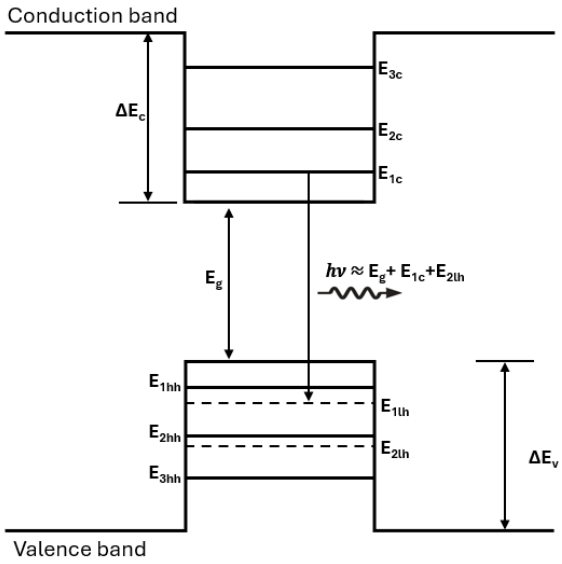

Figure 2.3 Illustration of the energy levels of quantized electrons, heavy holes (represented by solid dashes), and light holes (shown by dashed dashes).

2.1.2. Non-radiative recombination

Non-radiative recombination is a basic constraint on the efficiency of modern optoelectronic devices such as laser diodes (LDs) and light emitting diodes (LEDs). In comparison to radiative recombination, in which photons are emitted, there is no light emission in non-radiative recombination when electrons and holes recombine, instead releasing energy predominantly as heat through phonons. The most common forms of non-radiative recombination include Shockley–Read–Hall (SRH) recombination, which arises from trap states within the bandgap or defects in the crystal lattice. Auger recombination, which involves a three-carrier process, redistributing recombination energy to a third carrier, and surface or interface recombination. The Auger process in case of long wavelength lasers is the dominant nonradiative mechanism [26]. The band-to-band mechanism is the predominant form of auger recombination in longer-wavelength lasers. This occurs when two electrons collide, ascending one electron to a higher energy state in the conduction band while transitioning the other to valence band. When the high-energy electron finally relaxes to lower energy state in the conduction band, it releases the extra energy as heat to the crystal lattice [21]. In the heavy hole (HH) band, two holes may collide in an equivalent manner; in this mechanism, the hole that is pushed deeper into the valence band is moved to the split-off (SO) or light hole (LH) bands. The three different types of transitions, together termed Auger processes, are illustrated in Figure 2.4.

In this figure, LH, SO and HH stand for light-hole, split-off and heavy-hole bands, respectively and C is for conduction band.

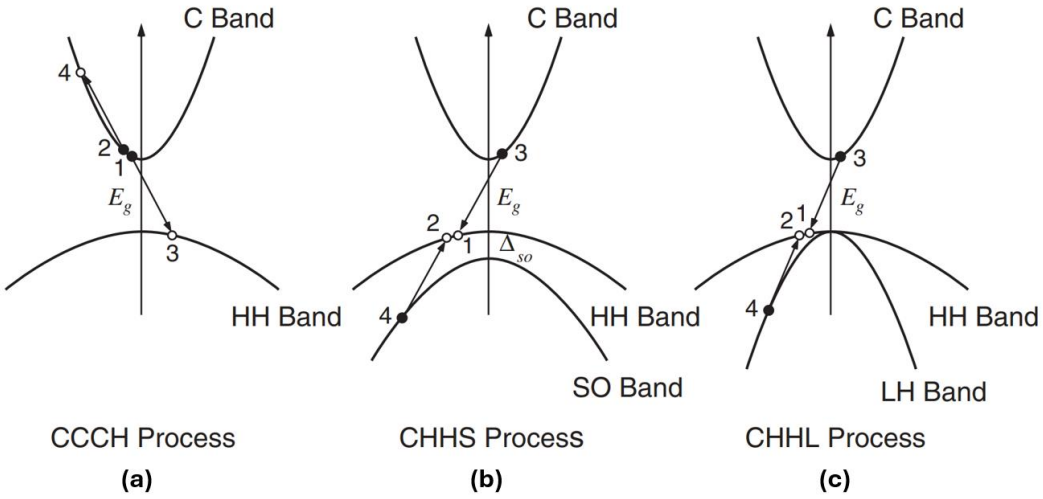

Figure 2.4 Auger recombination mechanisms in III–V semiconductors [21].

- In the CCCH process, from the first recombination, the energy is utilized to elevate an electron from one conduction band to a superior band. In this instance, one electron transitions from the C band to the C band, while the other transitions from the C band to the H band (H representing the HH band).
- The energy from the initial recombination in CHHS transfers an electron from the SO band to the HH band, resulting in a vacancy in the SO band.
- In CHHL, the energy from the first recombination transfers one electron from the light hole (LH) band to the heavy hole (HH) band, so creating a hole in the LH band

Nonradiative recombination reduces the density of carriers available for radiative transitions, thereby decreasing the laser's output power and lowering its differential quantum efficiency. Among the dominant nonradiative mechanisms, Auger recombination plays a critical role, especially at high carrier densities. As the Auger processes depend on carrier-carrier interactions, the Auger recombination rate, given by $R_{Auger} = CN^3 = \frac{I_{Auger}}{qV}$ increases rapidly with increase in carrier concentration [27], [28].

In semiconductor lasers, where carrier densities in the active region are approximately equal under steady-state conditions, all three Auger mechanisms CCCH, CHHS, and CHHL can contribute significantly to carrier loss. Moreover, the Auger recombination

increases exponentially with temperature for a given carrier density, further degrading laser efficiency at elevated operating temperatures [21], [27], [28].

This temperature dependance of Auger coefficient is given by [24]

$$C(T) = C(K)\ exp\left(\frac{-E_a}{kT}\right) \qquad 2.1$$

where E_a is the required energy for an Auger recombination, C the Auger coefficient, k is the Boltzmann constant and T is the temperature.

The Auger recombination rate increases with decrease in bandgap and is strongly dependent on the bandgap of material [27], [28]. In the CCCH Auger process, the hole'availability at state 3 in Figure 2.4 (a) is significantly enhanced in materials with a smaller bandgap, leading to an increased Auger recombination rate at a given carrier density Moreover, the initial electron states 1 and 2 in Figure 2.4 (a) lie closer to the conduction band edge in such materials, which results in a higher occupation probability at finite temperatures and further promotes the recombination process. Consequently, the Auger transition rate exhibits an exponential increase with decreasing bandgap energy [21].

For bulk narrow-gap III-V materials, in the case of the CCCH process, C is very large as the activation energy is low. QWs usually have a smaller Auger coefficient C [29]. The CHHL Auger process becomes significant at longer wavelengths where the bandgap energy E_g is smaller than the spin-orbit splitting energy E_Δ. Similarly, the CHHS Auger process rapidly diminishes in importance under the same condition, and the CHCC process becomes the dominant mechanism at longer wavelengths. In mid-infrared lasers, the spin-orbit splitting bandgap E_Δ is smaller than the bandgap E_g rendering the CHHS process energetically forbidden [30]. Consequently, the CHHL and CCCH Auger processes emerge as the primary nonradiative recombination mechanisms in mid-IR light-emitting devices.

Auger recombination does not contribute to the device's light output; instead, they increase the current needed to produce a population inversion and lasing behavior. The equation provides the basis for this increase [21],

$$I_{NRth} = \frac{qVCN_{th}^3}{\eta_i}\ exp[\frac{3\ (\alpha_m + \alpha_{int})}{\Gamma\ g_0}] \qquad 2.2$$

In this equation, g_0 differential gain parameter, Γ optical confinement factor, V active region volume, η_i internal quantum efficiency, α_m and α_i are mirror and internal cavity

losses respectively. The cubic dependence on the threshold carrier density N_{th} highlights that Auger recombination plays a major role in determining the total threshold current density. Consequently, an additional current component I_{NRth} is introduced by the nonradiative auger process, contributing not only to the current threshold but also to the operating current above threshold. This implies that a higher injection current ($I_{tot} = I_{th} + I_{NRth}$) is required both at and beyond threshold to maintain a given optical output power when Auger recombination is present. Furthermore, this increased current density leads to enhanced self-heating within the device, which in turn increases auger recombination, establishing a feedback loop that degrades overall efficiency and thermal stability.

2.2. Temperature effects on device performance

2.2.1. Carrier leakage over heterobarriers

A loss process known as carrier leakage occurs when carriers in a well layer can escape across a barrier and enter the confining layer, which consists of the barrier and the cladding. A schematic of QW's carrier leakage is shown in Figure 2.5. Carrier leakage can be affected by the height of the barrier and the mobility of electrons and holes. Holes are less mobile than electrons as they have large effective mass. As a result, the leakage electron is substantially more for a given band offset [14]. To escape from the quantum well, carriers acquire sufficient thermal energy, carrier leakage increases as the temperature rises. There is a correlation between carrier leakage from the active region of a semiconductor laser and both the threshold current and the internal quantum efficiency of the laser.

In case of quantum well lasers, the active region is confined specifically to the quantum well(s). However, under high injection or elevated thermal conditions, carriers may escape from the QW into adjacent regions. This includes both leakage into the surrounding waveguide layers and further into the doped cladding layers beyond the waveguide. Thermally excited holes can escape into the waveguide region from the quantum wells where they may undergo nonradiative recombination. This leakage process imposes a significant limitation on the output power [31] at room temperature, thereby degrading the overall performance of the diode laser.

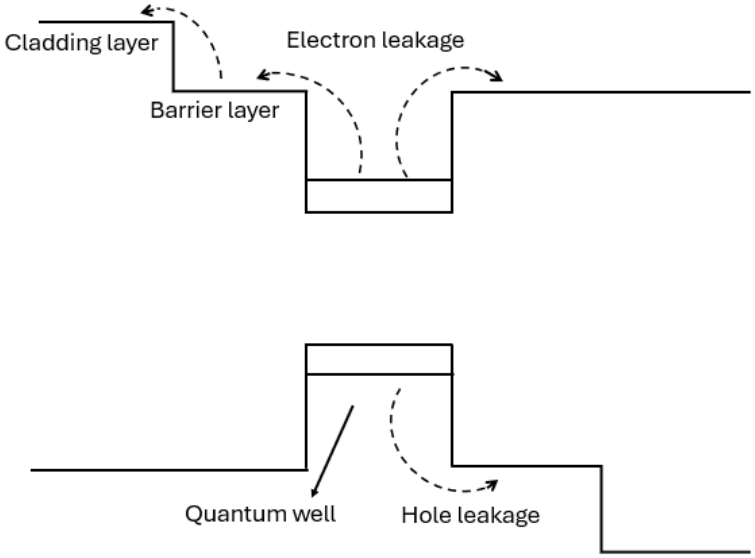

Figure 2.5 Carrier leakage into the barrier and cladding layers from quantum well.

2.2.2. Temperature dependence

As discussed earlier, temperature considerably affects the input current and the nonradiative threshold current. Equation 2.3 presents the threshold current, which incorporates additional temperature dependencies. As a function of temperature, the threshold current can be measured using equation 2.3 [21],

$$I_{th} = I_0 \quad exp(\frac{T}{T_0}) \tag{2.3}$$

where I_0 is the threshold current at 300K and T_0 is some overall characteristic temperature.

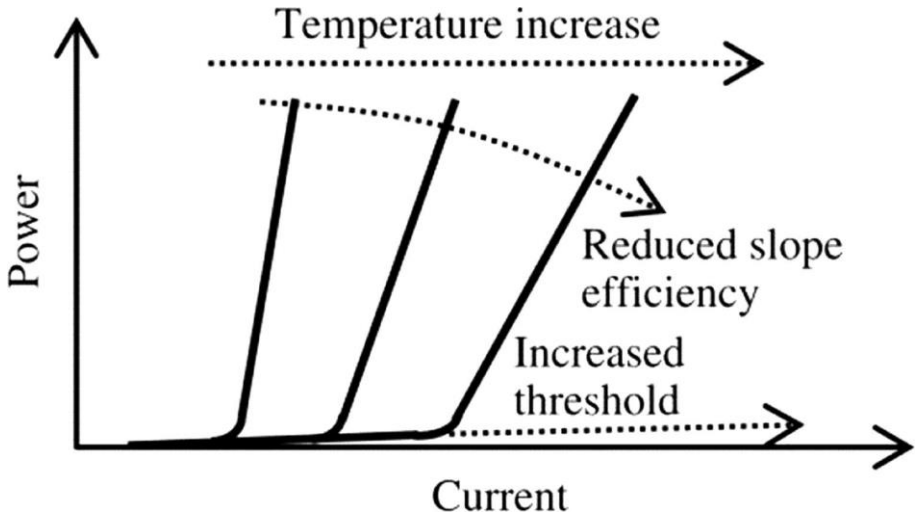

Figure 2.6 Output power versus input current for a laser diode operating at different temperatures [32].

As we can see in Figure 2.6, the laser threshold is strongly affected by the laser's temperature. As seen in figure, increased operation temperatures affect the threshold current by increasing it and also reduce slope efficiency and overall efficiency [32]. A lower value of the characteristic temperature signifies a stronger dependance of the threshold current to temperature (since $\frac{dI_{th}}{dT} = \frac{I_{th}}{T_0}$). Minor temperature-related fluctuations in other parameters can be efficiently integrated into this model within a constrained range of temperature. For instance, internal quantum efficiency may decrease at elevated temperatures owing to heightened current leakage or more intricate loss mechanisms. This internal efficiency decrease can be observed as a drop in the effective T_0, regardless of the precise nature of internal quantum efficiency's temperature dependence.

Threshold current and characteristic temperature have significant dependance of number of quantum wells in epitaxial structure. The higher carrier density in SQW causes the threshold current to be more sensitive to temperature, which is a disadvantage of SQW lasers. MQW devices exhibit enhanced thermal stability due to reduced carrier density in the quantum wells, resulting in small Auger recombination and internal losses [33].

2.3. Fabry-Perot cavity laser diode

Optical gain in a semiconductor can be enhanced by placing the gain medium within an optical cavity, as illustrated in Figure 2.7, which facilitates optical feedback. In this configuration, light undergoes multiple round trips between two mirrors, being amplified

during each pass through the gain region. Typically, one mirror M1 is highly reflective (close to 100%), while the other M2 is partially transmitting to allow emission of the output light. This type of resonant structure is referred to as a Fabry-Pérot cavity.

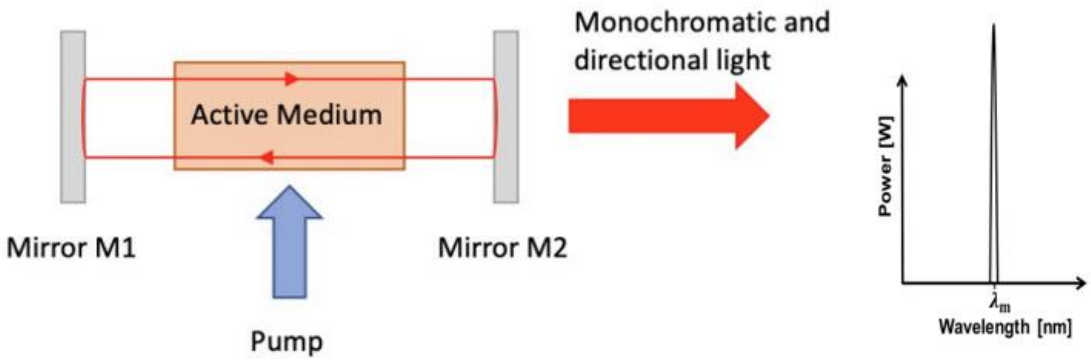

Figure 2.7 A Fabry-Perot Cavity giving monochromatic and directional light.

When the modal gain g_{mod} becomes equal to the total optical losses α_{total} with increased injected carrier concentration N, the laser threshold is then obtained [21], [22].

$$g_{mod} = \Gamma_{g_{th}} = \alpha_m + \alpha_{int} = \alpha_{total} \qquad 2.4$$

Where Γ is the optical confinement factor, which is the ratio of the optical field in the gain area to the overall optical field, g_{th} is the maximum gain for an injected carrier concentration *N,* α_{int} are internal losses and α_m are the mirror losses given by equation 2.5.

$$\alpha_m = \frac{1}{L} ln(\frac{1}{R_1 R_2}) \qquad 2.5$$

Equation 2.4 is satisfied for discrete set of frequencies and is given by,

$$\nu_m = \frac{mc}{2nL} \qquad 2.6$$

where ν_m is the cavity resonance frequency of longitudinal mode of a Fabry-Perot cavity having optical length nL. Consequently, the laser mode oscillates at a frequency corresponding to one of the longitudinal modes supported by the Fabry-Perot cavity. When the threshold condition described in equation 2.4 is met, the laser emits light at the wavelength defined by equation 2.6, as illustrated in Figure 2.7. Although an FP cavity supports multiple longitudinal modes shown in Figure 2.8, lasing occurs only for those modes where the optical gain compensates for the total cavity losses.

2.3.1. Output power and threshold current

Carrier and photon density rate equation for semiconductor lasers can be written as [21],

$$\frac{dN}{dt} = \frac{\eta_i I}{qV} - \frac{N}{\tau} - \nu_g g N_p \qquad 2.7$$

$$\frac{dN_p}{dt} = \Gamma \nu_g g N_p + \Gamma \beta_{sp} R_{sp} - \frac{N_p}{\tau_p} \qquad 2.8$$

The coupled rate equations describe both the steady-state and dynamic operation of a diode laser. In these equations, η_i denotes the internal quantum efficiency, defined as the fraction of injected carriers into active region that are successfully converted into photons within the device. The current injection applied to the laser terminals is represented by I, while q is the electron charge and V the volume of the active region, ν_g the group velocity, τ the carrier lifetime, , $N_p$the photon density, and τ_p the photon lifetime in the cavity, which is determined by optical losses. The spontaneous emission coupling factor is denoted by β_{sp}, and R_{sp} represents the rate of spontaneous photon generated.

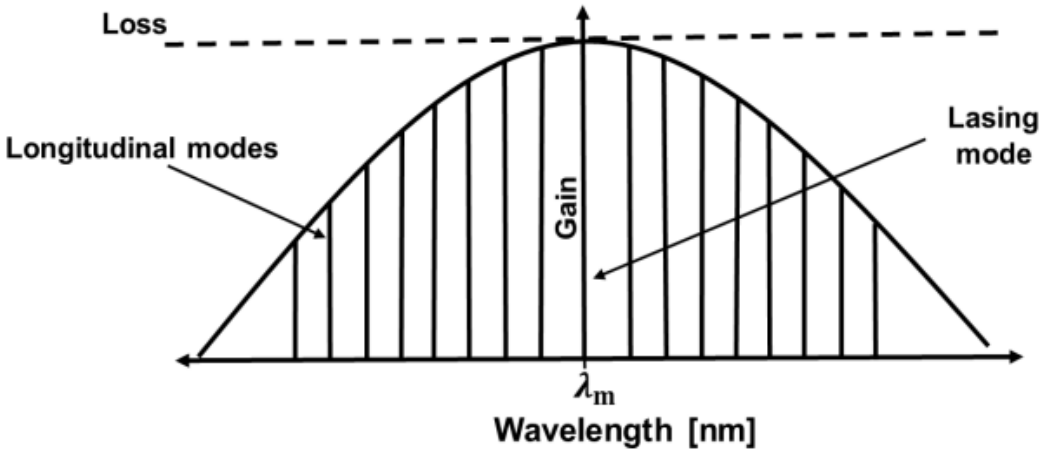

Figure 2.8 A semiconductor laser's longitudinal modes and gain curve are shown schematically.

In equation 2.7, the first term represents the rate of carrier injection into the active region. The natural decay of carriers in the absence of stimulated emission can be explained by the second term, while the third term accounts for stimulated recombination of electron–hole pairs. For light-emitting diodes (LEDs), the contribution of the stimulated recombination term can be neglected,

$$J = qd(AN + BN^2 + CN^3 + R_{st}R_{ph}) \quad 2.9$$

The injected current in equation 2.9 can be divided into three main contributions: spontaneous recombination, stimulated recombination, and non-radiative recombination processes. These mechanisms can be expressed as follows: the term BN^2 represents spontaneous radiative recombination, the term AN corresponds to non-radiative recombination associated with defects and trap states. The cubic dependence, CN^3, accounts for non-radiative auger recombination, while the final term describes the contribution from stimulated recombination d is the thickness of the active region.

LI characteristics

To obtain the diode laser's output power above threshold, one can solve steady state carrier rate equation 2.7, ($\frac{dN}{dt} = 0$), below threshold ($R_{st} \approx 0$), That is,

$$\frac{N}{\tau} = BN^2 + AN + CN^3 = \frac{\eta_i I}{qV} \quad 2.10$$

Rewriting the equation of threshold values,

$$\frac{N_{th}}{\tau} = BN_{th}^2 + AN_{th} + CN_{th}^3 = \frac{\eta_i I_{th}}{qV} \quad 2.11$$

Above threshold the density of steady state photon be calculated by substituting equation 2.10 into carrier rate equation 2.7,

$$N_p = \frac{\eta_i (I - I_{th})}{q v_g \, g_{th} V} \quad 2.12$$

Since the escape rate of photon out of the laser cavity is $v_g \alpha_m$, the power a diode laser emits above threshold is,

$$P_{out} = \eta_d \frac{h\nu}{q} (I - I_{th}) \quad 2.13$$

where $h\nu$ represents the energy of a photon and η_d corresponds to external differential quantum efficiency defined as the ratio of the total number of photons coming out of the device to the electron injected into the cavity, mathematically written as,

$$\eta_d = \frac{dP_{out}}{dI} \; \frac{2q\lambda}{hc} \quad 2.14$$

Equation 2.13 expresses the total optical power emitted through both facets of the Fabry–Perot cavity. For the case of mirrors with equal reflectivity, the output power is symmetrically distributed, with half of the total power emitted from each facet. Furthermore, according to equation 2.13, if optical gain, internal quantum efficiency, confinement factor, and cavity losses stay constant, the output power rises linearly when the current is beyond the threshold value.

For a semiconductor laser, the required threshold current can be expressed as [21],

$$I_{th} = \frac{qVBN_{tr}^2}{\eta_i} \; exp^{\frac{2(\alpha_m+\alpha_{int})}{\Gamma g_0}} \qquad 2.15$$

Here, N_{tr} denotes the transparency carrier density, defined as the carrier density at which the material gain exactly balances the absorption, and gain coefficient is g_0. This equation highlights that the threshold current is highly influenced by the mode confinement factor, the total optical losses, and the gain coefficient.

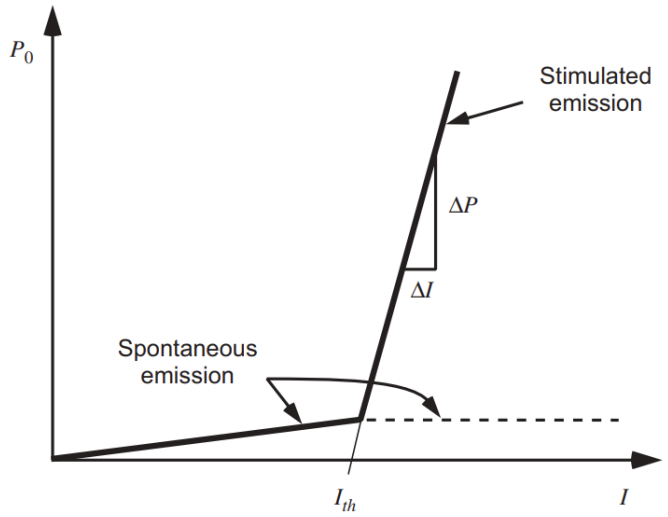

Figure 2.9 Schematic showing output power vs input current.

Figure 2.9 illustrates the output power versus input current (L-I) characteristic of a semiconductor laser, where below the threshold current I_{th} the output power arises primarily from spontaneous emission, and above I_{th} the slope changes sharply due to stimulated emission. The incremental slope efficiency is defined by the ratio $\Delta P/\Delta I$, which quantifies how effectively the injected current is converted into optical output power in the lasing regime.

2.3.2. Efficiency and losses of laser diode

The principal feature of a laser diode is its power-current (P-I) relationship, seen in Figure 2.9. The threshold current I_{th} can be ascertained from the observed P–I curve by locating the intersection of the linear region above the threshold with the current axis. With known emission wavelength, the differential quantum efficiency η_d using equation 2.14 can be calculated. The mirror loss α_m can be determined using equation 2.5. Nevertheless, the internal quantum efficiency η_i and the net internal optical loss α_i cannot be derived from observations of one single device.

These characteristics can be determined by employing multiple lasers with different cavity lengths, diced from the same processed material and identical mirrors. By measuring the differential efficiencies of devices with varying cavity lengths, the results can be expressed in terms of mirror losses, internal losses, and cavity length, as shown in equations 2.16 and 2.17 [21].

$$\eta_d = \frac{\eta_i \, ln(\frac{1}{R_1 R_2})}{L_1 \alpha_i + \, ln(\frac{1}{R_1 R_2})} \qquad 2.16$$

and

$$\eta_d' = \frac{\eta_i \, ln(\frac{1}{R_1 R_2})}{L_2 \alpha_i + \, ln(\frac{1}{R_1 R_2})} \qquad 2.17$$

where L_1 and L_2 represents the lengths of the laser diodes with different cavity lengths. Solving, we find

$$\alpha_i = \frac{\eta_d' - \eta_d}{L_1 \eta_d - L_2 \eta_d'} \, ln(\frac{1}{R_1 R_2}) \qquad 2.18$$

and

$$\eta_i = \eta_d \eta_d' \, \frac{L_1 - L_2}{L_1 \eta_d - L_2 \eta_d'} \qquad 2.19$$

Using equations 2.18 and 2.19 gives the desired internal parameters. However, there is uncertainty in the experimental data, it restricts the use of these equations. For improved reliability, it is preferable to use multiple data points and extract the unknown parameters through curve fitting. The optimal method in this case involves plotting the reciprocal of the measured differential efficiency against the cavity length L.

The linear fitting to the data yields a slope and intercept, enabling the determination of αi and ηi. Specifically,

$$\frac{1}{\eta_d} = \frac{1}{\eta_i}\left[1 + \frac{\alpha_i}{ln\left(\frac{1}{R_1 R_2}\right)} L\right] \qquad 2.20$$

Thus, the intercept provides η_i , which can be used in the slope to calculate α_i.

2.4. Gallium arsenide material systems

2.4.1. Lattice structure

Semiconductors are characterized by a periodic crystal arrangement that extends throughout the solid, referred to as a lattice. Most III–V compound semiconductors, such as gallium arsenide (GaAs), exhibit a zincblende structure, characterized by a face centered cubic (fcc) lattice. This configuration is achieved by positioning an extra atom at a displacement of x/4 + y/4 + z/4 from each atom of the face-centered cubic sublattice, where x, y, and z are the basis vectors of the cubic cell. Figure 2.10 illustrates the zincblende crystal structure of GaAs, in which each arsenic atom is covalently bonded to its four nearest gallium atoms in a tetrahedral coordination.

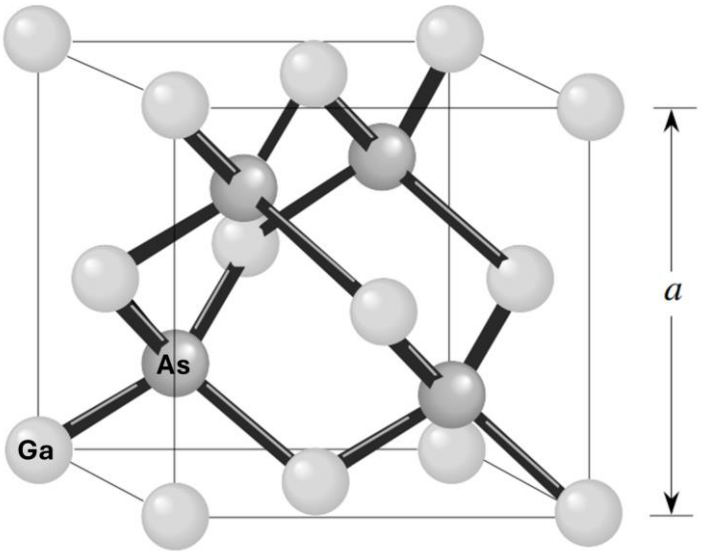

Figure 2.10 GaAs Zincblende structure [19].

The length of a side in a cubic unit cell is called lattice constant ‘a’. This length is same in all three dimensions. To grow the materials epitaxially on a monocrystalline substrate, this parameter plays a key role in the process. Either the crystal structure of the substrate

should be adopted by the new material that is growing on the substrate, or the new material should have the same lattice constant as the substrate material.

2.4.2. Defects in semiconductor lattice

Defects in semiconductor crystals may arise either from thermodynamic factors during growth or from the incorporation of unintentional impurities into the lattice. In general, crystalline defects are classified into four main categories: (i) point defects, (ii) line defects, (iii) planar defects, and (iv) volume defects. Each class of defect perturbs the periodicity of the crystal lattice and can adversely influence the electrical and optical properties of the material. Since such imperfections degrade the performance and reliability of electronic and optoelectronic devices, minimizing their formation is of critical importance in semiconductor fabrication.

Point defects

Point defects are localized disruptions in the lattice involving one or a few atomic sites. There are a variety of point defects, as shown in Figure 2.11 [19]. Such defects can act as nonradiative recombination centers, thereby reducing carrier lifetime and device efficiency.

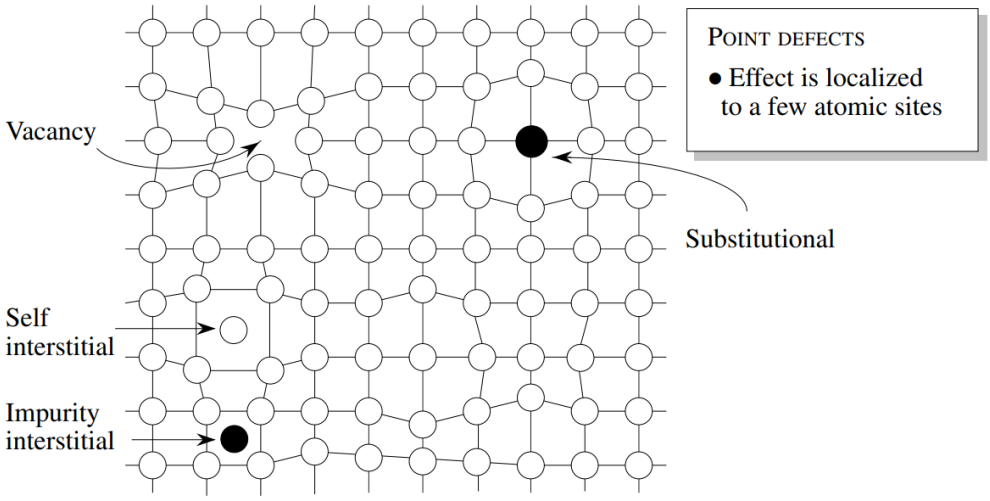

Figure 2.11 Point defects in semiconductor crystal lattice [19].

A important point defect in compound semiconductors such as GaAs is the antisite defect, in which a gallium atom occupies an arsenic lattice site rather than its normal gallium site. These defects (commonly represented as Ga_{As}) can act as recombination centers and consequently degrade device performance.

Line defects or dislocation

Unlike point defects, line defects commonly referred to as dislocations extend over a series of atomic sites that can be connected along a line Dislocations may arise, for instance, when an additional half-plane of atoms is introduced or removed from the crystal lattice as shown in Figure 2.12 [19], leading to what is known as an edge dislocation. They may also be generated by slip processes in which atomic planes shift, causing bonds to break and reform at new positions.

Dislocations present a critical challenge in semiconductor materials, particularly in the fabrication of strained layer heterostructures. In optoelectronic devices, the presence of dislocations introduces nonradiative recombination centers, which can drastically degrade performance and, in severe cases, render the device nonfunctional. Hence, minimizing dislocation density is essential for achieving high-performance and reliable semiconductor lasers.

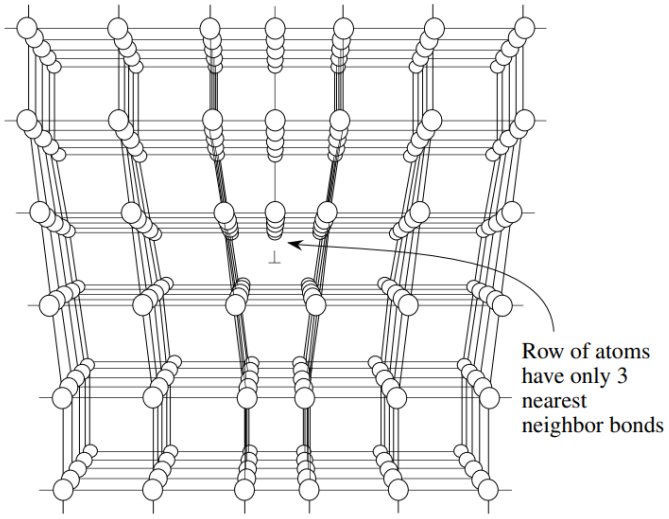

Figure 2.12 A diagram illustrates the existence of a dislocation [19].

2.4.3. Heterostructues

When a material having a crystal structure similar to that of the substrate is epitaxially deposited, it typically adopts the same lattice arrangement as the underlying substrate. However, semiconductor devices often consist of heterostructures composed of different material layers. To preserve monocrystallinity, the lattice constants of these layers must be closely matched to that of the substrate. While ultrathin layers of lattice-mismatched

materials can be accommodated elastically, once the layer thickness exceeds a critical value h_c, the accumulated strain relaxes through the formation of misfit dislocations. These defects disrupt crystal symmetry and significantly degrade the structural and electronic quality of the heterostructure.

The critical thickness is primarily governed by the degree of lattice mismatch, although the elastic properties of the constituent materials also play a role. A larger lattice constant difference between the epitaxial layer and the substrate results in a smaller critical thickness, thereby increasing the likelihood of dislocation formation [34].

2.4.4. Strained QW layers

When a material is grown on a substrate with a different lattice constant in a heterostructure, the resulting unit cell adopts altered dimensions. When deposited on the substrate, the unit cells of this material undergo deformation: they are stretched under compressive strain or compressed under tensile strain, depending on whether their natural lattice is larger or smaller than that of the substrate. Once the critical thickness, h_c, exceeds the limit, dislocations begin to occur, and the strain increases with the addition of each consecutive layer of lattice-mismatched material.

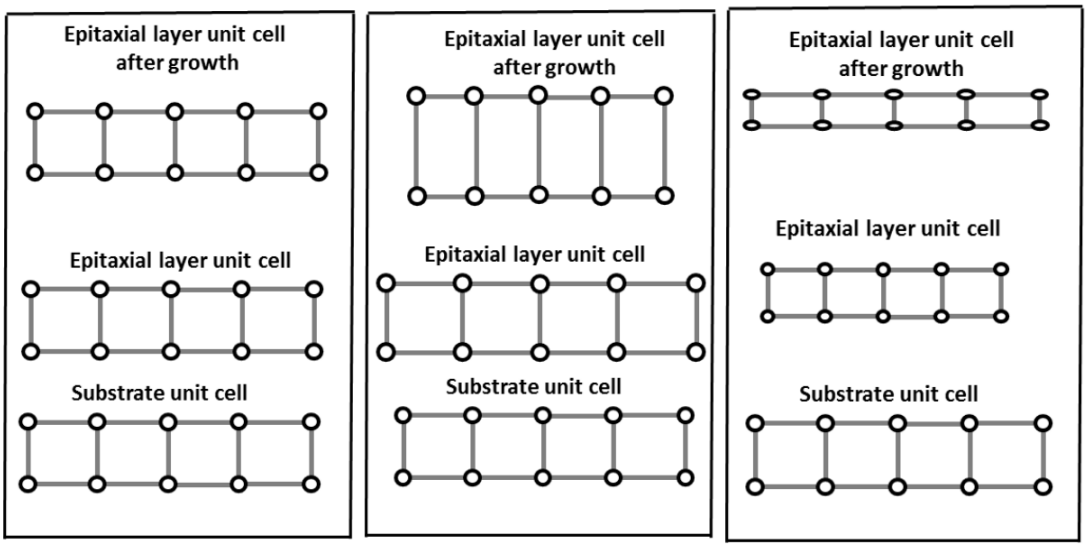

Figure 2.13 Schematic illustration of unit cell deformation in an epitaxial layer due to lattice mismatch with the substrate.

In lattice-mismatched materials, a strained layer whose thickness remains below the critical limit can positively impact device performance. Strain, for example, increases the separation between the heavy- and light-hole subbands, which reduces the auger

recombination coefficient [16]. Beyond lowering the threshold current and modifying the bandgap, strain also effects the device performance [24].

2.4.5. GaAs, AlGaAs and InGaAs based semiconductor alloys

GaAs, which crystallizes in the zincblende structure and has a lattice constant of 5.6533 Å, is classified as a direct bandgap semiconductor. The bandgap of intrinsic GaAs for bulk arsenic is E_g=1.424 eV, corresponding to a photon wavelength of λ_{ph}= 0.868 µm, calculated using $\lambda_{ph}= hc/E_g$. However, when doping is introduced to the crystals, the bandgap narrows, resulting in an increase in wavelength [35].

Along with GaAs, this work employs ternary compounds such as InGaAs for quantum wells and AlGaAs for the waveguide and cladding layers, with the compositions adjusted by varying the Ga–In and Al–Ga ratios. The lattice constants and other relevant parameters of these arsenide materials are summarized in Table 1.

Table 1 Some important parameters of III-V semiconductors at room temperature [19]

Substance	Lattice constant (Å)	Bandgap Energy (eV)	Wavelength (nm)	Refractive Index (n)
GaAs	5.6533	1.424	870	3.59
AlAs	5.6620	2.16	Indirect gap	2.98
InAs	6.0583	0.354	3500	3.72

Table 1 shows that the lattice constants of GaAs and InAs differ sufficiently little to allow bandgap engineering by adjusting the composition of ternary alloys. Lattice matching can also be achieved using Vegard's law, an empirical approximation stating that the lattice constant of a semiconductor alloy varies linearly with the composition of its constituent elements. For ternary alloys such as InGaAs and AlGaAs, the lattice constant can be expressed as:

$$a(In_xGa_{1-x}As) = x\, a_{InAs} + (1-x)\, a_{GaAs} \qquad 2.21$$

The bandgap energy of ternary materials can be estimated in a manner analogous to the lattice constant, with the inclusion of an additional parameter known as the bowing

constant “C”. For instance, the bandgap energy of InGaSb can be determined using the following quadratic relation:

$$E_g(In_xGa_{1-x}As) = x\,E_{g,InAs} + (1-x)E_{g,GaAs} - Cx(1-x) \qquad 2.22$$

In III–V semiconductors, the bowing parameter *C* is positive, which means the actual alloy bandgap is lower than the value predicted by a linear interpolation.

2.4.6. InGaAs quantum well

For emission around 940 nm, in this work we used InGaAs quantum wells (QWs) grown on GaAs substrates. Since the lattice constant of InAs is significantly larger than that of GaAs, the incorporation of indium into GaAs always results in compressively strained QWs. To achieve emission at 940 nm, the indium composition is carefully adjusted so that the strain remains below the critical thickness limit, thereby avoiding misfit dislocations [36]. Strain in the QW can be engineered by varying the indium concentration: increasing indium content lowers the bandgap and extends the emission wavelength, while keeping the thickness sufficiently thin.

The compressive strain in InGaAs QWs is advantageous for laser operation because it enhances hole confinement in the valence band, reduces threshold carrier density N_{th}, and increases differential gain $\frac{dg}{dN}$ [36]. However, as the emission wavelength approaches the longer end of the near-infrared spectrum, the valence-band offset between the QW and GaAs barriers decreases, which can cause leakage of holes across the heterointerface thereby greatly increasing J_{th}. Therefore, careful optimization of indium composition and well thickness is essential to balance strain, confinement, and material quality for efficient 940 nm edge-emitting lasers.

3. Edge-emitting laser diode

This chapter aims to discuss the primary design and operation of edge-emitting laser diodes (EELs), focusing on elements that can be enhanced via epitaxial growth and device fabrication. It establishes a basis for comprehending the correlation among material design, fabrication, and device performance.

All semiconductor lasers comprise a gain region, where stimulated emission transpires, and a resonator that provides optical feedback. According to the resonator configuration, the laser may emit light laterally, as observed in edge-emitting lasers (EELs), or vertically, as seen in vertical-cavity surface-emitting lasers (VCSELs). For numerous applications, including fiber-coupled sensing, it is crucial for the laser to function in a steady single optical mode. The epitaxial structure in EELs largely determines the transverse mode, which is perpendicular to the junction plane, whereas device processing, such as ridge generation, current confinement, and index-guiding techniques, can regulate the lateral mode, which is parallel to the junction plane [22].

3.1. Waveguide modes

The optical field distribution inside the laser cavity is determined by the refractive index profile and layer geometry. Waveguiding in edge-emitting lasers can be analyzed along three main directions: transverse, lateral, and longitudinal.

3.1.1. Transverse modes

Transverse confinement occurs in the vertical direction through the layered heterostructure [37]. The refractive index difference between the active region and cladding layers determines the optical confinement factor, which has a strong impact on both the threshold current and the modal gain. By choosing the active layer thickness d to satisfy the condition in equation 3.1, a double-heterostructure semiconductor laser can be designed to emit in a single vertical mode, perpendicular to the junction plane.

$$d < \frac{\lambda}{2}(n_2^2 - n_1^2)^{\frac{1}{2}} \qquad 3.1$$

where n_1 and n_2 are the refractive indices of cladding and active region. For all guided modes, the inequality $n_2 > n_e > n_1$ is satisfied.

3.1.2. Lateral modes

Lateral confinement is achieved through gain guiding or index guiding, depending on the device design. It defines the number of supported lateral modes and strongly impacts beam quality and far-field divergence.

Gain guiding

In gain-guided devices, the lateral confinement of the optical mode arises from localized optical gain within the active region. This gain, governed by carrier injection, can be expressed as,

$$g = g_d\,(N - N_{tr}) \qquad 3.2$$

Here, g denotes the optical gain, g_d the differential gain, N the carrier density, and N_{tr} the transparency carrier density. The optical field is confined to regions of high gain, allowing lateral guiding without requiring a ridge-waveguide (RWG) structure. Vertical confinement, in contrast, is consistently maintained by index guiding through the epitaxial layer design.

A major limitation of gain guiding is that the injected current is not strictly confined within the active layer, unlike in index-guided RWG devices. As a result, a portion of the injected carriers does not contribute efficiently to population inversion, which leads to higher threshold currents. For this reason, gain guiding is typically employed in devices designed for high-power operation, where multimode behavior is acceptable.

In gain-guided lasers, the optical gain present in all laser structures serves as the main mechanism for confining the optical mode within the junction plane [5]. These devices are termed gain-guided because the spatial distribution of the optical mode along the junction is determined by the gain profile.

The simplest current-limiting configuration for a gain-guided laser is the oxide stripe device [23]. In this design, an insulating oxide layer defines a contact stripe through which current is injected into the laser structure. The insulating layer is typically silicon dioxide (SiO_2), which is why gain-guided lasers of this type are also called stripe-oxide lasers. Figure 3.1 shows a schematic of a stripe-oxide gain-guided laser. Compared to index-guided lasers, stripe-oxide gain-guided devices are relatively easier to fabricate.

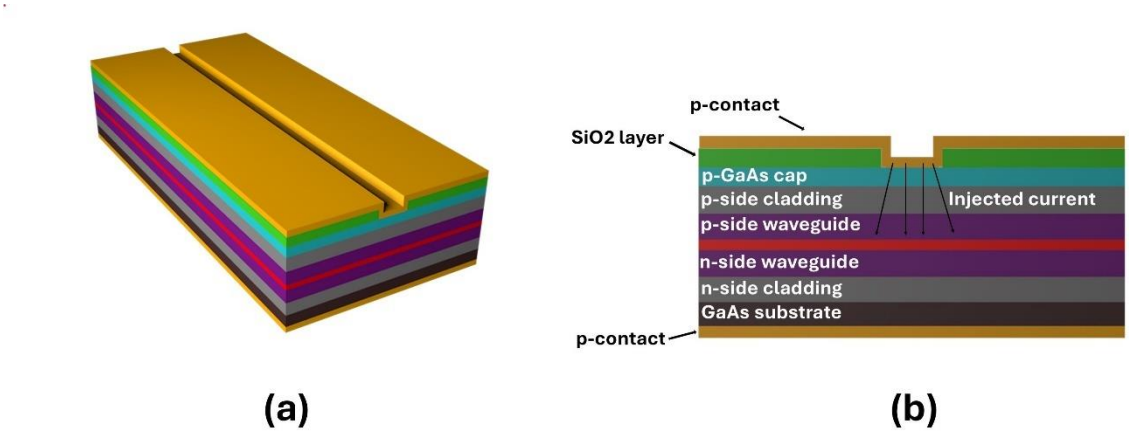

Figure 3.1 Schematic depiction of gain guided GaAs based oxide stripe laser. (a) Isometric view of laser device (b) Cross sectional view

Performance of device

There are two significant limitations in the performance of gain-guided lasers. The effective current density reduces when thr current spreads in the layers other than active layer [38]. In semiconductors, the refractive index decreases as current density increases, resulting in a reduced effective index step and thus a decrease in lateral confinement [39]. Due to the absence of an effective lateral index in gain-guided lasers, anti-guiding is significantly pronounced in these devices. These two limitations contribute to elevated threshold current and diminished external differential quantum efficiency in these laser types.

The kinks in the light-current (L-I) characteristics of gain-guided lasers can arise from the carrier leakage due to current spreading and other device or material related non-idealities. Such kinks can result from the excitation of higher-order modes, a transition from transverse electric (TE) to transverse magnetic (TM) polarization, or lateral shifts of the optical mode [22]. Despite these challenges, stripe-oxide lasers remain strong candidates for high-power multimode operation.

3.2. Far field profile

A semiconductor diode laser emits light with an elliptical cross-section, as illustrated in Figure 3.2. As the beam propagates away from the laser facet, it undergoes divergence, and the resulting angular intensity distribution observed at a large distance is referred to as the far field (FF). Since the waveguide is only a few hundred nanometers thick in the vertical direction, strong diffraction occurs vertically. In contrast, the larger lateral dimension results in a much smaller beam divergence along the horizontal axis.

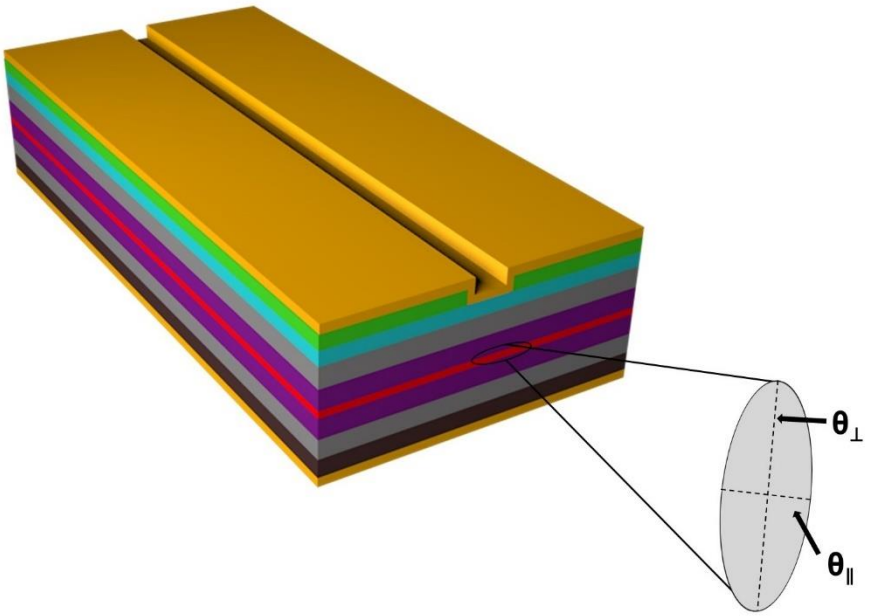

Figure 3.2 Far field of oxide stripe laser diode.

The far-field width is determined by drawing lines from the active region of the crystal to the ends of the ellipse's major or minor axis. The angle formed between these lines represents the angular spread at which the intensity falls to 50% of its maximum. The full width at half-maximum (FWHM) angles, $\theta_{\parallel}$ and $\theta_{\perp}$, correspond to the directions parallel and perpendicular to the junction plane, respectively, as shown in Figure 3.2. These angles are essential for characterizing the laser mode's angular distribution and offer insights into the degree of modal confinement. In general, a very small $\theta_{\parallel}$ signifies weak lateral confinement of the optical mode. For optimal coupling to an optical fiber, a nearly symmetrical output beam profile is preferred, as it helps minimize coupling losses [40].

4. Fabrication and simulation

This chapter presents the numerical simulation of GaAs-based epitaxial structures for 940 nm edge-emitting lasers (EELs), alongside a detailed description of the fabrication process used to realize oxide-stripe devices with different cavity lengths. By combining simulation with experimental fabrication, this chapter establishes a direct link between theoretical design and practical realization of high-performance 940 nm edge-emitting lasers. This integrated approach not only validates the predictive capability of simulation tools but also provides a robust framework for guiding future developments in semiconductor laser.

4.1. Device processing

The fabrication of the edge-emitting semiconductor laser was carried out through a photolithographic process step. All procedures were performed in a cleanroom environment under strict contamination control, as the device involves micro-scale features where even minor impurities can severely compromise performance. The major steps done for fabrication are schematically illustrated in Figure 4.1.

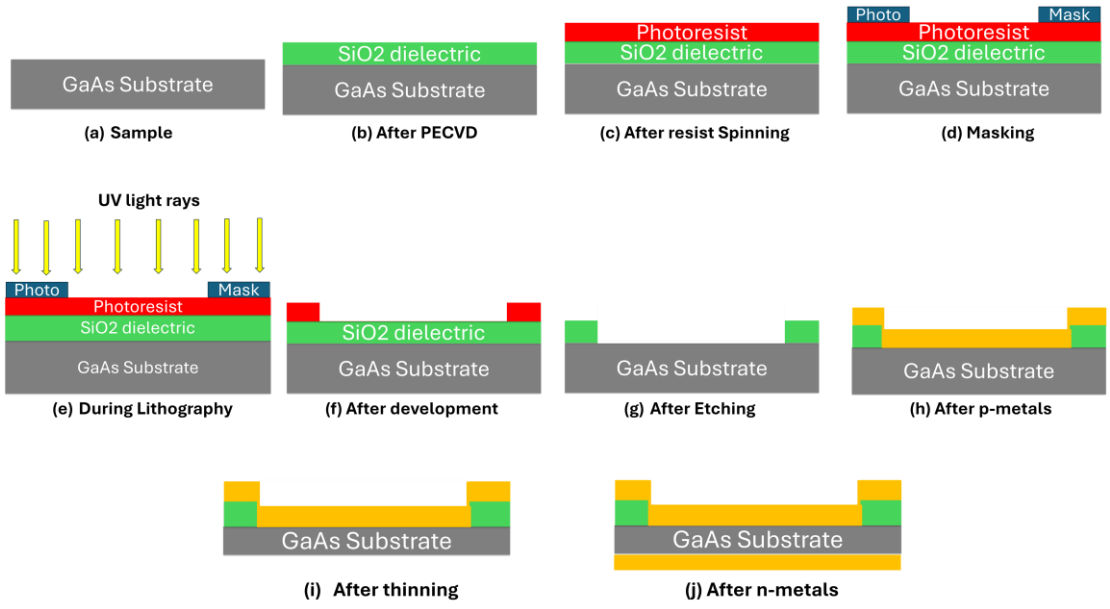

Figure 4.1 Schematic illustration of all major steps done for fabrication of one edge emitting oxide strip device.

For process development, instead of employing a complete wafer, which is both costly and unnecessary at this stage smaller wafer pieces were utilized. The complete epitaxial

structure used in this thesis is detailed in section 4.2.1, which summarizes the parameters imported for the growth specification sheet.

4.1.1. Plasma enhanced chemical vapour depsotion

PECVD is a plasma-assisted chemical vapor deposition technique in which highly reactive radicals generated in the plasma migrate toward the substrate and adhere to its surface, forming a uniform dielectric film. This method is widely used in semiconductor processing due to its excellent film uniformity and step coverage.

In the present study, a 150 nm SiO_2 layer was deposited using plasma-enhanced chemical vapor deposition (PECVD). SiO_2 served as the insulation layer in the fabrication of the edge-emitting laser diodes. The deposition was carried out by placing the samples in a PECVD chamber equipped with a heated electrode maintained at approximately 300 °C. The resulting plasma-assisted chemical reactions enabled the controlled growth of the insulating SiO_2 layer on the wafer surface.

4.1.2. Photoresist coating and UV-lithography

The lithography process starts by coating the sample surface with an ultraviolet (UV)-sensitive photoresist. This photoresist contains a photoactive compound (PAC) that undergoes a chemical reaction upon exposure to UV light, changing its solubility in an alkaline developer solution. In a positive photoresist, the exposed areas become more soluble and are removed during development, while in a negative photoresist, the exposed areas become less soluble and remain after development.

The resist is applied by spin coating, where a small droplet of resist is dispensed onto the center of the wafer mounted on a rotating chuck. As the sample spins at high speed, the liquid spreads uniformly across the surface, forming a thin, controlled film. The resist thickness can be adjusted by tuning the spin speed and duration.

Before resist application, the surface is primed with hexamethyldisilazane (HMDS), which removes residual moisture and improves adhesion between the resist and the substrate. Once coated, the resist layer is subjected to a soft bake on a hotplate to partially harden the film, hence changes the resist profile’s behavior during development. Care must be taken to avoid excessive baking, as over-hardening may inhibit proper development of the exposed regions.

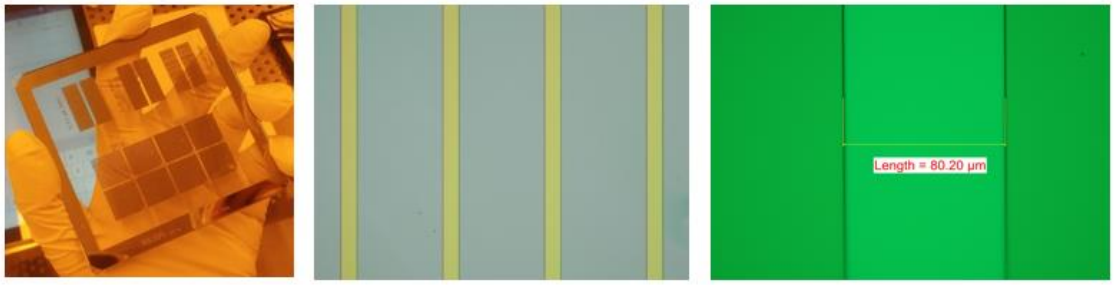

Figure 4.2 (a) Glass plate bearing the original patterned mask design (b) Developed mask patterns on the sample following lithographic processing (c) Magnified view of the transferred patterns, showing a measured line width of 80.20 µm; caused by the exposure and development.

Patterning is carried out using UV photolithography with a mask aligner (Suss MA6). The mask is a glass plate as shown in Figure 4.2 (a) containing metal features created via electron-beam lithography. During exposure, UV light passes through the transparent regions of the mask, altering the solubility of the underlying photoresist. The required exposure time depends on the resist type and the critical feature size. After exposure, the wafer is developed in a solution that selectively removes the defined regions. Careful optimization of the process is essential to prevent under- or over-development, which can degrade pattern fidelity.

After development, the patterned resist is inspected under a microscope to ensure accurate feature transfer as shown in Figure 4.2 (b). Finally, a hard bake is carried out to enhance adhesion and mechanical stability of the resist, allowing it to withstand subsequent processing steps such as etching. In Figure 4.2 (c), we can see the actual developed pattern of width 80.20 µm.

4.1.3. Dielectric etching

In many semiconductor processes, the transfer of the ridge pattern into the dielectric layer is achieved by reactive ion etching (RIE), a dry etching technique capable of producing highly anisotropic profiles [41], [42]. RIE combines physical sputtering by inert gas ions with chemical reactions of reactive gases to achieve directional etching. While this method is widely used for high-precision dielectric etching, it can also induce surface damage to the underlying semiconductor, particularly GaAs, which may degrade optical and electrical properties [43].

In the present work, however, the transfer of the ridge pattern to the SiO_2 dielectric layer was performed using wet chemical etching. Specifically, buffered hydrofluoric acid (BHF)

was employed due to its high selectivity for SiO_2 and its negligible etching effect on GaAs. While wet etching facilitates the efficient removal of the oxide mask, BHF can cause surface damage on the GaAs substrate, and over-etching presents a significant issue that requires precise controlling.

Although wet etching is inherently isotropic or anisotropics and can result in undercutting beneath the resist mask, in this application it provided a reliable method for SiO_2 removal. The ability of HF-based solutions to etch oxides without significantly attacking GaAs ensures clean and well-defined stripe openings required for oxide stripe laser fabrication.

Compared to RIE, which is commonly employed for oxide etching in semiconductor technology, wet etching was deliberately chosen as it is fast, but in the meantime it also leaves traces of etchant on the surface.

4.1.4. Electrical contacts

Prior to forming electrical contacts, the samples were subjected to a native oxide removal step by immersing them for 20 seconds in a dilute solution of ammonium hydroxide and deionized water ($NH_4OH:H_2O$, 1:10). This wet etching treatment ensured the removal of surface oxide, thereby providing a somehow clean semiconductor surface for metal deposition.

The metal contacts for the oxide stripe laser process were deposited using electron beam evaporation inside a high-vacuum chamber. The e-beam evaporator system used for metal deposition in this work is equipped with a multi-pocket crucible holder that allows up to eight different metal sources to be used sequentially without breaking vacuum. A tungsten filament acts as the electron source, which, when heated by an applied current, emits electrons. These electrons are accelerated under a high voltage (typically 10 kV) and magnetically directed towards the target material. The focused electron beam locally heats and evaporates the metal, producing a flux of atoms that condense onto the sample surface, forming uniform thin films.

For the p-side metallization, a trilayer metal stack was used, consisting of Ti/Pt/Au with thicknesses of 50/50/250 nm, respectively. Titanium was employed as the adhesion layer to promote good bonding between the semiconductor surface and the subsequent metallic layers. Platinum acted as a diffusion barrier, preventing intermixing between gold and the semiconductor material, while the top gold layer provided a stable, oxidation-resistant, and highly conductive contact surface. The relatively thick Au layer

was particularly important to ensure low series resistance and robust electrical performance of the device.

After thinning and polishing the n-side of the wafers (as described in the section 4.1.5), n-contact metallization was carried out using a multilayer stack of Ni/Au/Ge/Au with thicknesses of 5/5/30/90 nm. In this metallization scheme, nickel can reduce native surface oxides and it also prevents the formation of Ni-Ga-As compounds that can facilitate Ge incorporation during alloying. Germanium (Ge) acts as a donor to heavily dope the contact region, lowering resistance and mitigating Schottky barrier effects to enable reliable ohmic contacts, and the final thick gold layer acts as a stable, highly conductive overlayer.

4.1.5. Chemical-mechanical polishing

The typical dimensions of an individual oxide stripe laser chip are around (1600 × 500) µm². Cutting the wafer into such small chip sizes is not feasible unless the substrate is thinned to a reduced thickness of about 110-120 µm. To achieve this, a combination of mechanical grinding and chemical etching is employed. Prior to the thinning process, the p-side of the wafer is protected by first spinning a resist layer on the surface and then sealing it with a layer of wax for better adhesion to the glass substrate to proceed with chemical mechanical polishing.

4.1.6. Rapid thermal annealing

Following the n-side metallization, the samples underwent a rapid thermal annealing (RTA) step to activate the ohmic contacts. The purpose of this treatment is to promote interdiffusion between the gold and Germanium layers, resulting in the formation of a eutectic alloy. This process enables germanium to diffuse further into the GaAs substrate, thereby lowering the contact resistance and significantly improving the quality and stability of the n-type ohmic contact after RTA [41].

In this work, annealing is carried out using the contact RTA system. The sample is placed n-side down between two silicon carbide (SiC)-coated wafers, and the process is performed under an inert nitrogen atmosphere to prevent oxidation. Controlled heating is applied according to the defined recipe, ensuring reproducibility and uniform treatment across the sample surface.

4.1.7. Packaging

Dicing and mounting

After completing the RTA, the sample is cut into individual emitters. A fine scribe is made along the junctions between adjacent laser diodes (LDs), and mechanical strain is applied to cleave the bar along these lines, isolating single devices. Due to their small size, the LDs are mounted onto aluminum nitride (AlN) submounts, which facilitate handling and act as heat spreaders to dissipate thermal energy from the active region, improving device performance. The attachment is performed using the electrically conductive, thermosetting adhesive EPO-TEK MED-H20E, which hardens upon heating.

Wire bonding

Gold wires are used to connect the top of the chip to the submount. The tip of the gold wire is melted using an electrical arc and then gently pressed onto the top of the laser diode (LD), while the other end is secured to the submount. Figure 4.3 (a) shows the schematic of wire bonded chip on the AlN submount and Figure 4.3 (b) is the SEM image of the packaged device.

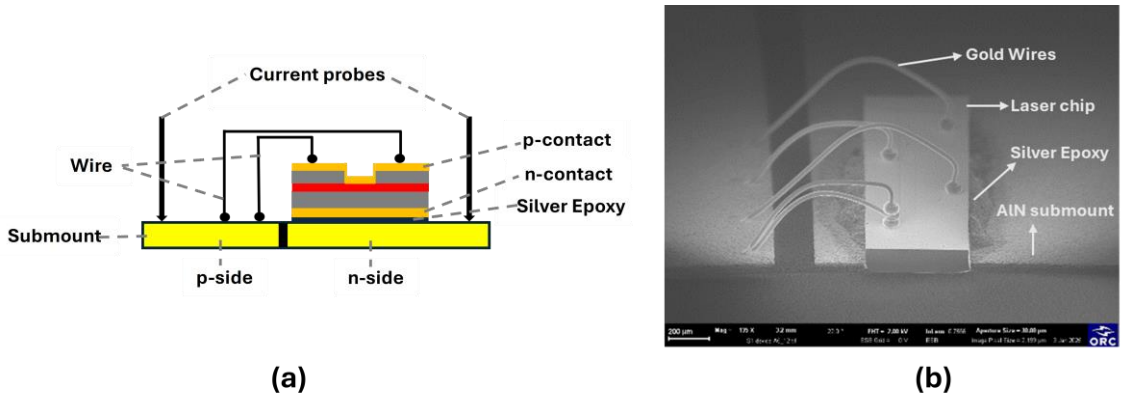

Figure 4.3 (a) wire bonding and (b) SEM image of an oxide stripe component bonded on a submount for measurements.

4.2. Introduction to HAROLD

HAROLD, standing for Hetero-structure Laser Diode Model, is heterostructure simulator developed by Photon Design Ltd., optimized for the design of both edge emitting lasers (EEL) and VCSEL quantum-well lasers. Its advanced physical simulation environment supports arbitrary vertical layer architectures, allowing accurate modeling of epitaxial structures with quantum wells, graded layers, and complex compositions

HAROLD provides integrated electro-optical-thermal simulations, solving Poisson's equation, drift-diffusion carrier transport, current dispersion, waveguide mode confinement, thermal conduction, and optical amplification in 1D or 2D setups. These linked simulations facilitate a coherent characterization of edge-emitting laser behavior, especially where temperature-dependent material characteristics and current distribution affect device performance.

The Figure 4.4 shows the epitaxial structure editor of the HAROLD laser simulator used to define the vertical layer stack for the edge-emitting device. The left pane (“Total Structure”) lists the full sequence from the top metal contact to the substrate. The red highlighted layer is the InGaAs quantum well, whose properties are edited in the right pane. Doping for the well is set to zero, and default SRH and meshing policies are selected. At the bottom, the auto calculated simulation wavelength (≈ 0.978 μm) and temperature (300 K) are specified for computing material parameters (refractive index, absorption, gain) used in the subsequent optical/electrical and loss-budget simulations. All layers thicknesses are listed in the Figure 4.5.

Figure 4.4 HAROLD epitaxial structure editor for the simulated GaAs/AlGaAs edge-emitting laser.

4.2.1. Epitaxial layer structure

A GaAs substrate was introduced as the foundation layer with a thickness of 350 µm with n-type doping of 3×10^{-18} cm^{-3}. On top of this substrate, $Al_{0.70}GaAs$ cladding layers of 0.7µm were added on both sides of the active region, with one n-doped and other p-doped to provide the required carrier injection. Between the claddings, a series of confinement and quantum well layers were defined. The confinement barriers consisted of $Al_{0.25}GaAs$ with thicknesses of 0.7 µm, while the active region was formed with $In_{0.13}GaAs$, separated by barriers to ensure quantum confinement. The epitaxial layer sequence thicknesses used to simulate is schematically illustrated in Figure 4.5, showing the arrangement of substrate, cladding, waveguide, quantum wells, and contact layers.

The epitaxial structure used in this work follows a conventional double heterostructure laser design with an InGaAs quantum well as the active region. On the p-side, heavily doped GaAs contact layers are introduced to provide low-resistance ohmic contacts, followed by a digital grading layer where the aluminum composition is gradually reduced from 70% to 0%, that smooths the bandgap transition between the high Al cladding and the waveguide. The p-AlGaAs cladding layer, with high aluminum content, provides strong optical confinement, while the adjacent AlGaAs waveguide layers with lower Al content guide the optical mode towards the active region.

GaAs	150 nm p-side contact 2
GaAs	50 nm p-side contact 1
AlGaAs	20 nm p-side digital grading
AlGaAs	700 nm p-side cladding
AlGaAs	300 nm p-side waveguide
InGaAs	5 nm quantum well
AlGaAs	300 nm n-side waveguide
AlGaAs	700 nm n-side cladding
AlGaAs	20 nm n-side digital grading
GaAs	200 nm n-side buffer layer
GaAs	3500 µm n-side buffer layer

Figure 4.5 GaAs based epitaxial structure grown using MBE

The core of the device consists of a thin InGaAs quantum well sandwiched between GaAs barriers, where radiative recombination occurs and the emission wavelength is

defined. On the n-side, the structure is mirrored with an AlGaAs cladding, a digital grading layer, and a GaAs buffer layer that ensures lattice quality and a smooth transition to the GaAs substrate, which provides mechanical stability and the n-type electrical contact. This proposed laser design is to ensure efficient carrier injection, strong optical confinement, and minimized interface defects.

4.2.2. Laser structure

Quantum well (QW) lasers can be categorized into three types based on the band alignment at the well–barrier interface: type-I (nested), type-II (staggered), and type-III (broken gap) [28]. In type-I structures, electrons and holes are both confined within the same layer, whereas in type-II and type-III designs, the carriers are separated across neighboring layers, leading to indirect radiative recombination. Since a detailed analysis of the band structure is beyond the scope of this thesis, it will not be addressed further.

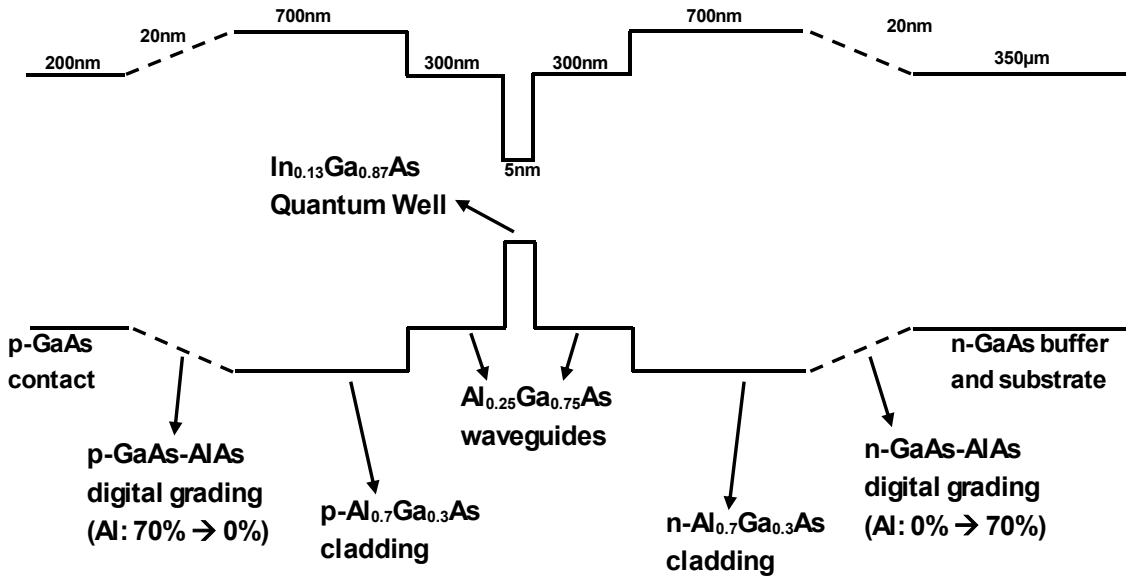

Figure 4.6 Band diagram of type-I laser structure, left portion is the top layer and the right most part is the bottom layer.

The laser structure in Figure 4.6 is type-I with $In_{0.13}Ga_{0.87}As$ QW based on the layer thicknesses presented in Figure 4.5. The emission of $In_{0.13}Ga_{0.87}As$ QW is at 940nm wavelength. The band alignment of quantum well and barriers forms nested alignment using $In_{0.13}Ga_{0.87}As$ QW for all composition range with $Al_{0.25}Ga_{0.75}As$ barriers.

In addition, ternary alloys offer advantages from a growth perspective. This laser structure itself is fabricated by molecular beam epitaxy (MBE) on an n-doped GaAs substrate. The growth begins with a buffer layer, a few hundred nanometers thick,

composed of GaAs to match the substrate material and provide a high-quality surface for the subsequent epitaxial layers.

The intrinsic region includes a compressively strained quantum well that serves as the active area, providing the laser gain. Surrounding $Al_{0.25}G_{0.75}As$ layers function as waveguides, confining the optical field. This confinement arises because, as shown in Table 1, layers with higher aluminum content exhibit lower refractive indices. For the laser structure illustrated in Figure 4.5 and Figure 4.6, the corresponding refractive index profile and optical mode distribution are presented in Figure 4.7

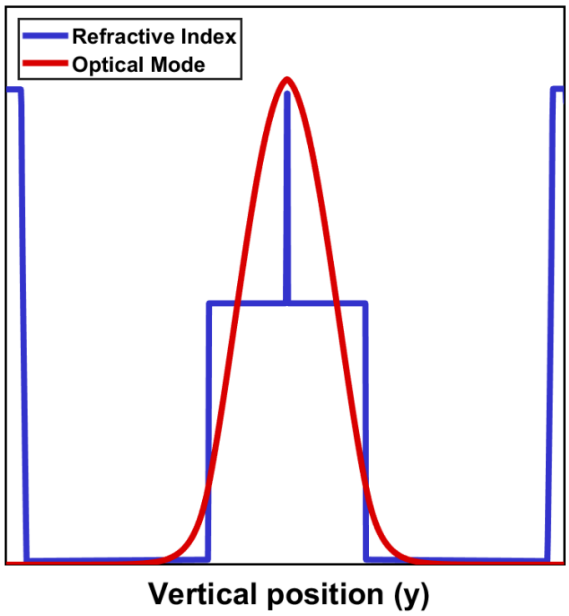

Figure 4.7 Optical mode intensity (red curve) and Refractive index profile (blue curve) for the laser structure.

4.2.3. Band profiles in equilibrium and forward-biased operation

Vertical conduction- and valence-band edges across the epitaxial stack are shown in Figure 4.8 that forms the separate-confinement heterostructure with a single quantum well at its center.

For the laser structure presented in Figure 4.6, with no external bias as depicted in Figure 4.8 (a), the Fermi level is uniform, and the bands are piecewise flat within each layer, exhibiting step changes at every heterointerface that reflect the band-offsets between the well and its barriers/claddings. The quantum-well region appears as a local minimum in the conduction band and a corresponding local maximum in the valence band, providing strong confinement for electrons and holes, respectively. Mild band bending

occurs in the doped claddings near the junction due to built-in fields, while the abrupt “kinks” at interfaces indicate abrupt composition changes and the partitioning of the offset between the conduction and valence bands. In this state, carriers remain localized by the offsets and there is negligible net current; leakage paths over the barriers are energetically suppressed.

Figure 4.8 (b) shows the heterostructure under forward bias, the bands tilt across the stack, dropping on the electron-injection side and rising on the hole-injection side. Quasi-Fermi levels split, enabling substantial carrier injection into the well. The tilting reduces the effective barrier height on the injecting side and slightly increases it on the opposite side, so carriers drift/diffuse toward the well where they accumulate and recombine radiatively. Local screening in the well partially flattens the bands there, while the surrounding barriers continue to limit thermionic escape and field-assisted leakage. The resulting profile is characteristic of an operating edge-emitting heterostructure laser: carriers are confined to the active region, which sustains population inversion and optical gain, while residual tilting sets the balance between confinement, leakage, and series-resistance heating.

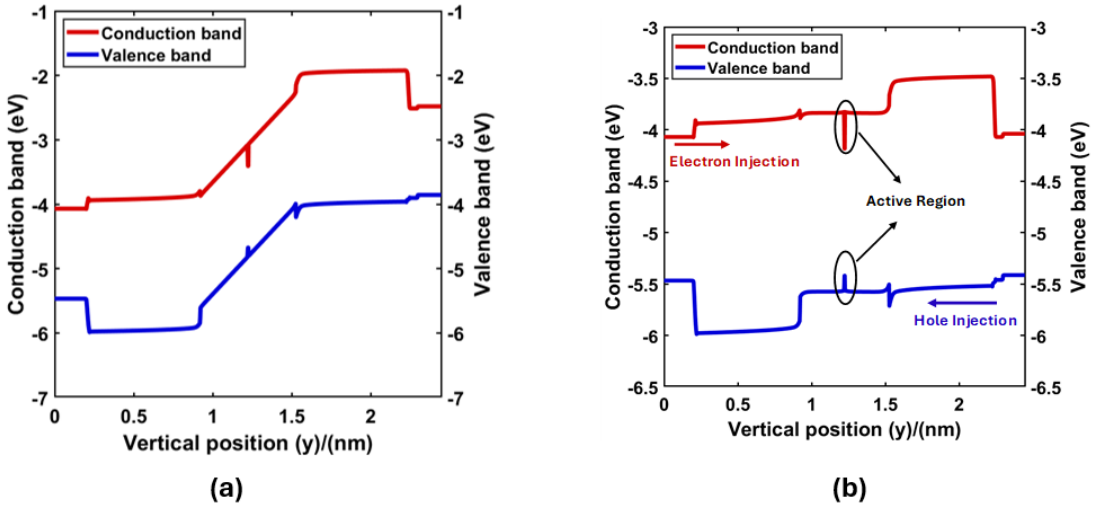

Figure 4.8 Simulated band-edge profiles of the epitaxial double-heterostructure edge-emitting laser. Red and blue traces show the conduction- and valence-band edges across the vertical stack. (a) At equilibrium and (b) Under forward bias.

4.2.4. ILV characteristics of the simulated structure

In simulator panel the device is driven up to a maximum injection current of 1 A while recording the electrical (I-V) and optical (L-I) characteristics as shown in Figure 4.9.

The series resistance can be obtained from the slope dV/dI in the linear region above threshold. Using the segment between 100 and 800 mA, the calculated value is $R_s = 0.14\ \Omega$. From the L-I trace, the maximum optical power at 1 A is 1.1 W.

The L-I curve exhibits a kink (change in differential slope) at current around 220mA. Because the I-V remains featureless at the same current, this kink is optical not electrical in origin.

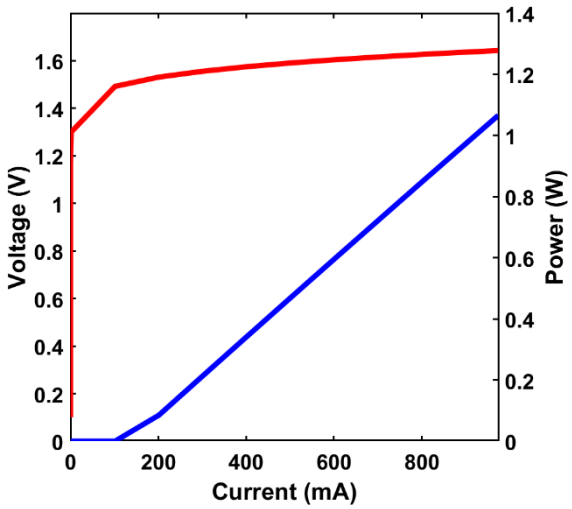

Figure 4.9 ILV characteristics of designed structure in self-heating operation.

Physically, forward bias splits the quasi-Fermi levels as discussed in section 4.2.3 and carrier fills the quantum well; above threshold the output follows. A kink corresponds to a change in differential efficiency caused by the waveguide/gain distribution:

- With rising current, carrier- and thermo-optic index changes reshape the vertical/lateral profile. This can trigger modal redistribution or a mode hop (e.g., from a higher loss to a lower loss lateral/vertical mode, or between longitudinal mode clusters), producing a jump in external differential efficiency.
- The loss-budget analysis supports this: internal losses that scale with current-FCA, metal/substrate absorption, and other “excess” parasitics, depend on how the optical field overlaps doped and lossy layers. A modal shift that pulls the field away from those regions reduces α_i and increases η_d, yielding the observed upward change in L–I slope.

4.2.5. Loss mechanisms

The total input power by is nearly 1.6 W and the output power from IL curve in the Figure 4.9 can be seen to be 1.1 W, which gives us an estimation that almost 0.5 W of power is being lost in the form of heat. Figure 4.10 presents the current-dependent power budget of the device, decomposed into the explicitly modeled channels (non-radiative recombination, Joule, free-carrier absorption, substrate/metal absorption, and the Thomson thermoelectric term) together with the cumulative total.

The total dissipated power rises nearly linearly with current, but consistent with the recombination physics outlined in section 2.1.2., the non-radiative recombination channel is the dominant sink over the entire operating range. As carriers are injected and the quasi-Fermi levels separate, recombination pathways that do not produce useful photons convert the electrical input directly into heat. At low injection this is primarily defect-assisted SRH recombination in and around the quantum well; at higher injection the Auger contribution grows and maintains the dominance of the non-radiative term.

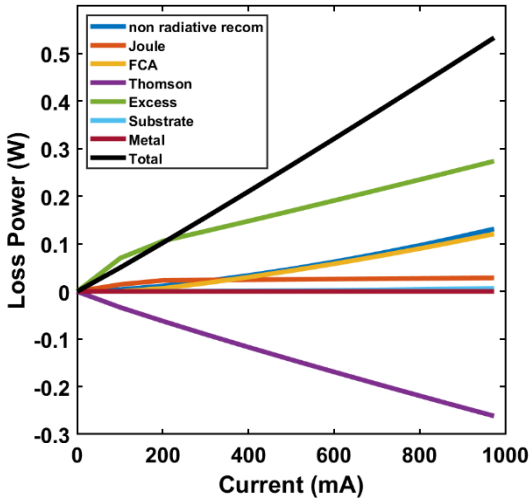

Figure 4.10 Power-loss budget vs current for the edge-emitting laser: total (black) and components, with excess as dominant losses

The excess-power heat source accounts for residual dissipation arising from uncoupled spontaneous emissions and scattered stimulated emissions that are reabsorbed as heat. Although this term appears significant in the Figure 4.10, the fabricated device is predominantly limited by non-radiative recombination losses. By comparison, Joule heating increases with current but remains secondary, indicating a moderate series resistance consistent with the smooth I-V trace. FCA and substrate/metal absorption are minor, reflecting limited modal overlap with doped and metallic regions due to the

heterostructure design. The Thomson term is negative, providing a thermoelectric cooling offset that does not change the overall conclusion.

4.2.6. Molecular beam epitaxy growth

After performing simulations with HAROLD and obtaining the expected device characteristics, the designed wafers were fabricated using molecular beam epitaxy (MBE). MBE is a highly controlled epitaxial growth technique in which crystalline layers are deposited onto a substrate such that the grown layers replicate the substrate's lattice structure. This method enables fabrication of extremely thin layers with nanometer precision, including quantum wells (QWs), which are essential for tailoring the optical and electronic properties of semiconductor lasers.

Growth takes place in an ultra-high vacuum (UHV) environment, where beams of atoms or molecules evaporated from elemental sources heated in effusion cells, impinge on the heated substrate. The substrate temperature is carefully controlled to provide sufficient thermal energy for the atoms to incorporate into their proper lattice sites. Since epitaxial growth requires close lattice matching between the substrate and deposited layers, binary GaAs substrates were used in this work. By adding additional elements during growth, ternary alloys (e.g., InGaAs) can be realized to adjust laser properties and meet the design requirements predicted by simulations. A schematic of the MBE growth chamber is illustrated in Figure 4.11

Within the growth chamber, precise control of layer composition is achieved by adjusting the temperature of individual sources and operating mechanical shutters that regulate the molecular beams. Typical III-V MBE systems include sources for gallium, indium, and aluminum (group III), arsenic, phosphorus, and antimony (group V), as well as dopants such as beryllium, silicon, carbon, or tellurium.

Semiconductor layers can be precisely doped during MBE to tailor their electrical conductivity by incorporating controlled amounts of impurities. For III-V arsenides like GaAs, tellurium (Te) typically serves as a donor dopant on group V sites to provide electrons, while beryllium (Be) acts as an acceptor on group III sites to generate holes. In this work, all GaAs substrates were n-doped with tellurium and oriented along the (100) plane. The GaAs substrate thickness is 350 μm, and the total thickness of the grown wafers is between 500 μm and 600 μm.

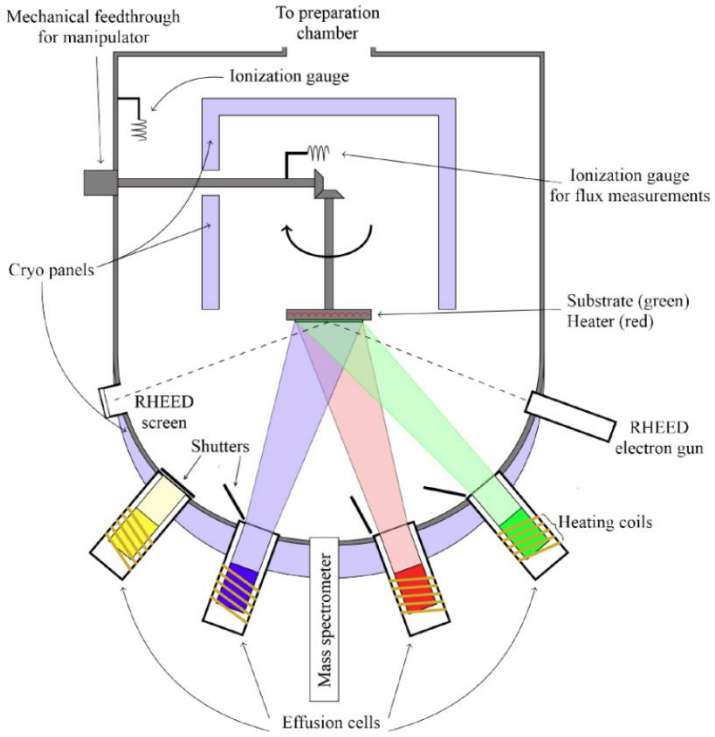

Figure 4.11 The schematic of a growth chamber of a typical MBE system from the inside [44].

5. Characterization results

This chapter discusses the methods employed to characterize the devices investigated in this thesis, along with the corresponding results. Edge-emitting laser diodes were analyzed by measuring their optical output and extracting key parameters from the resulting ILV characteristics, including the threshold current, peak power, slope efficiency and saturation current. Additionally, far field and spectral measurements were performed, and parameters such as external and internal quantum efficiencies, optical mirror losses, and threshold temperature were determined.

5.1. Experimental setup

To ensure consistency across all measurements, the devices were maintained at room temperature (25 °C) using a thermoelectric cooler (TEC) controlled by a temperature electronic controller.

ILV (current-light output power-voltage) measurements are used to characterize the optical and electrical performance of the device. In this method, the laser is driven over a range of injection currents while simultaneously recording the emitted optical power and the voltage across the gain section. From the resulting ILV curves, several important device parameters can be extracted, providing valuable insight into both the efficiency and the operating behavior of the laser.

The device's emitted light is directed into an integrating sphere and measured by a photodetector. The inner surface of the integrating sphere is coated for high reflectivity, allowing the incoming light to be uniformly redistributed through multiple reflections before reaching the detector port. This arrangement reduces the effect of beam shape or spatial distribution on the measured signal, ensuring accurate power measurements. The photodetector is chosen based on the device's emission wavelength to maximize detection efficiency.

5.2. ILV measurements

Figure 5.1 presents the electrical and optical performance of two laser diodes fabricated from epitaxial structures with different Al compositions in the waveguide layers: 12% Al and 25% Al. The comparison covers (a) current–voltage (IV) characteristics, (b) continuous-wave (CW) light-current (L-I) measurements, and (c) pulsed light-current measurements.

In Figure 5.1 (a), The IV characteristics of both devices exhibit the expected exponential dependence at low injection currents, transitioning into a quasi-linear regime at higher drive levels. Across the measured range (0-1 A), the device with 25% Al in the waveguide consistently requires a slightly higher forward voltage (1.1-1.75 V) compared to the 12% Al device. This behavior can be attributed to the increased bandgap and larger heterojunction offsets introduced by the higher Al content, which raise the built-in potential and contribute to a marginally higher series resistance. From the linear regime above ~200 mA, the extracted differential resistance is ~0.45 Ω for the 25% Al device and ~0.40 Ω for the 12% Al device. The value for 25% Al device has a good comparison with the simulation results as discussed in the section 4.2.4. The higher resistance of the 25% Al structure is therefore consistent with the modified band alignment and carrier transport properties, a trend that has also been reported in AlGaAs-based edge-emitting lasers where elevated Al fractions slightly increase the voltage requirement but are favorable for optical performance [45].

Under CW operation, the device with 25% Al in the waveguide demonstrates a bit better performance compared to the 12% Al device, exhibiting both a lower threshold current and a higher slope efficiency as shown in Figure 5.1 (b). By extrapolating the linear portion of the L–I curve, the threshold current is estimated to be ~160 mA for the 25% Al device versus ~210 mA for the 12% Al device. In the linear regime between 300-900 mA, the slope efficiency reaches ~0.45 W/A for the 25% Al device, in contrast to ~0.33 W/A for the 12% Al device, corresponding to approximately 35% higher slope efficiency and ~25% lower threshold current. At 1A drive current, the maximum output power of the 25% Al device approaches ~380 mW, compared to ~270 mW for the 12% Al structure. The improved performance can be attributed to two main factors: (i) the larger bandgap of the 25% Al waveguide reduces internal optical loss by suppressing parasitic absorption near the lasing wavelength, and (ii) the increased refractive-index contrast between waveguide and cladding enhances optical confinement in the active region, thereby improving modal gain and external efficiency. These advantages outweigh the modest increase in drive voltage observed in the IV characteristics, confirming that higher Al content in the waveguide yields superior CW output characteristics.

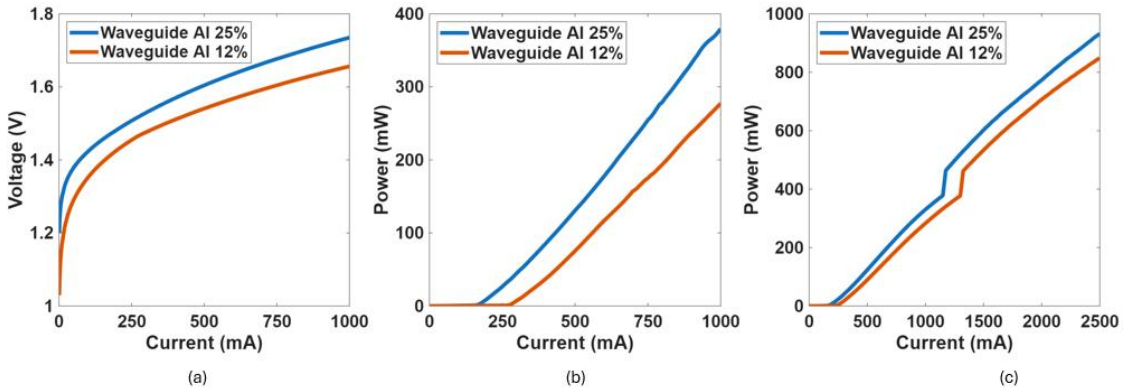

Figure 5.1 Comparison of (a) IV, (b) CW IL and (c) Pulsed IL curves for the edge emitting lasers having different Al compositions in waveguide.

In Figure 5.1 (c), we can see the pulsed L–I measurements further verify the better performance of the 25% Al device compared to the 12% Al device. Across the entire current range up to 2.5 A, the 25% Al waveguide consistently delivers higher output power, reaching ~950 mW versus ~870 mW for the 12% Al structure. Both devices exhibit nearly parallel slopes at high injections, but the 25% Al device provides a clear power advantage, particularly in the mid-current regime. The apparent “kink” observed around 1.3-1.4 A is not intrinsic to device operation but results from a measurement artifact, caused by the range switching of the integrating sphere system, which introduces a discrete saturation in the recorded power. Excluding this artifact, the pulsed data show that the 25% Al device sustains approximately 10% higher output power at elevated current densities, confirming its very minor improvement in gain-to-loss balance, reduced carrier leakage, and lower internal loss.

The 25% Al-composition wafer is selected for further cavity length studies because it demonstrates superior optical output under both CW and pulsed conditions, indicating reduced carrier leakage and lower internal losses. This improved performance makes it an ideal candidate for detailed evaluation of internal quantum efficiency and external differential quantum efficiencies, characteristic temperature (T_0), mirror losses, spectrum, and far-field properties, thereby providing a more reliable platform for optimizing device design and performance metrics.

Figure 5.2 shows the ILV curves for the different cavity lengths diced from 25% Al epi wafer. The IV curves in Figure 5.2 (a) demonstrates that shorter cavity devices (e.g. 500 µm) require significantly higher voltage at a given current compared to longer cavity lengths. This is due to increased series resistance and enhanced self-heating in short cavities, which drive up voltage drop and degrade carrier injection efficiency [46]. As the

cavity length increases, the current density for a given total current fall, reducing resistive and thermal losses, leading to a smoother, lower-voltage IV characteristic.

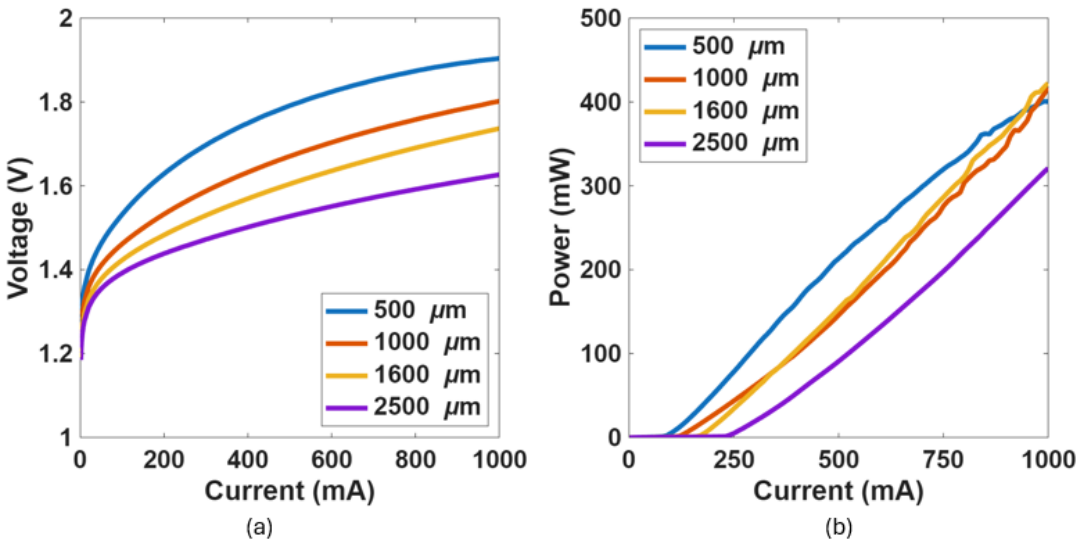

Figure 5.2 Comparison of (a) IV curves and (b) CW IL curves for the different cavity length 25% Al devices.

CW IL curves for the same devices are shown in Figure 5.2 (b). Shorter cavities show lower threshold currents and at the same time reduced output power at a given current due to increased optical losses and reduced gain volume.

5.3. Internal efficiency and losses

The internal quantum efficiency η_i, quantifies the fraction of injected electron–hole pairs that are converted into photons within the active region of a semiconductor laser, with the remainder lost through non-radiative channels. In this study, η_i is extracted via the cavity-length method. First, the slopes of the LI curves for 25% Al devices of identical cross-section but differing cavity length L are compiled in Table 2 these slopes are used to compute the external differential efficiency η_d according to equation 2.14. Next, the inverse efficiencies $1/\eta d$ are plotted against L and fit with a straight line, as shown in Figure 5.3 consistent with the standard linear relation in equation 2.20.

Table 2 Slope efficiency, external differential quantum efficiency, and its reciprocal for GaAs edge-emitting lasers with varying cavity lengths

Cavity Length	**Slope Efficiency (2 mirrors)**	**External Differential Quantum Efficiency**	
L (μm)	$2\frac{\Delta P}{\Delta I}$ **(mW/mA)**	η_d **(%)**	$\frac{1}{\eta_d}$
500	0.98	74	1.35
1000	1.04	79	1.27
1600	0.96	71	1.40
2500	0.80	61	1.63

The least-squares fit of $1/\eta d$ versus L yields an intercept $1.023636=1/\eta i$, giving $\eta i \approx 97\%$ by solving equation 2.20, for R=0.31, the internal losses for the used epi wafer are α_i = 2.7 cm^{-1}. These values are consistent with prior GRINSCH InGaAs QW results reported in the literature. For example, Coldren et. al. [21] report for 50 μm-wide $In_{0.2}Ga_{0.8}As$ GRINSCH lasers α_i = 3.2 cm_{-1} and η_i = 89.6%. Our epi (In ≈ 13%) yields α_i = 2.7 cm^{-1} and $\eta_i \approx 97\%$, i.e., comparable order of magnitude with a lower internal loss and a slightly lower internal efficiency. The small discrepancies are reasonable given differences in well composition (13% vs 20% In), layer design/fabrication, and measurement conditions, and they support the conclusion that the present wafer exhibits material quality broadly in line with established GRINSCH InGaAs QW benchmarks.

5.4. Characteristic temperature T_0

The characteristic temperature T_0 measures a laser diode's thermal sensitivity: higher T_0 means threshold current changes more slowly with temperature, i.e., better stability. Care is needed below room temperature for non-hermetic devices due to condensation and possible short circuits. Conventional AlGaAs lasers often show $T_0 \geq 120$ °C. As noted in Section 2.3.2, temperature strongly affects operating and non-radiative threshold currents; here we determine T_0 for our devices.

For 1600 μm cavity length device, we measured LI characteristics at several heat-sink temperatures as depicted in Figure 5.4. The resulting I_{th} and then calculated ln (J_{th}) values are compiled in Table 3.

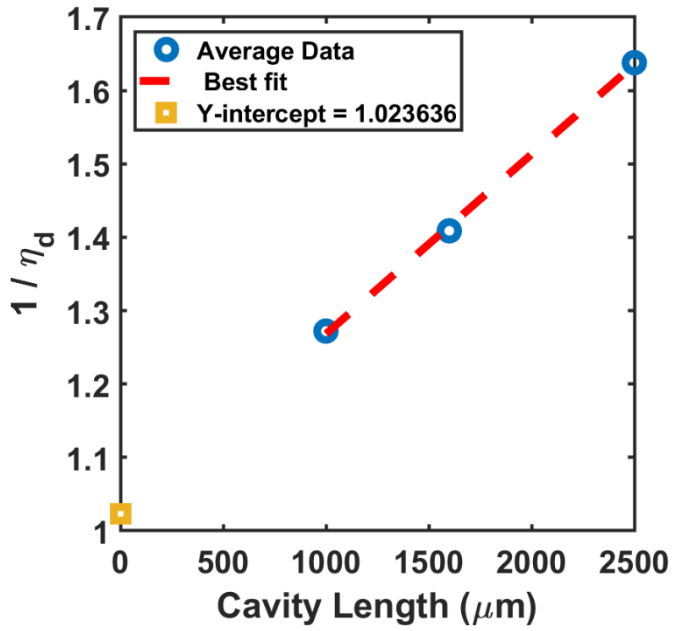

Figure 5.3 Inverse external differential efficiency 1/ηd versus cavity length L of 25% Al devices. The vertical-axis intercept gives 1/ηi (internal differential efficiency). The slope is proportional to the internal loss, with αi=slope x ηi x ln(1/R), R is the facet reflectivity (for cleaved GaAs/AlGaAs, R≈0.31).

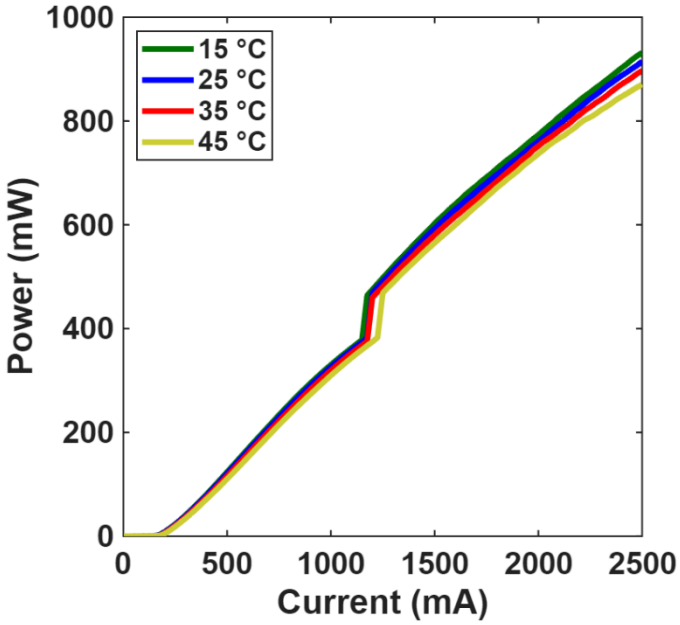

Figure 5.4 Output power versus current curves for 25% Al, cavity length 1600μm A4 device operating at various temperatures.

Table 3: A list of parameters of 25% Al device for T_0 calculation.

Temperature	**I_{th}**	**J_{th}**	**ln (J_{th})**
(ºC)	**(A)**	**(A/cm^2)**	
15	0.150	117.19	4.764
25	0.175	136.72	4.918
35	0.185	144.53	4.973
45	0.200	156.25	5.051
Length = 1600µm, Stripe width = 80µm, Area = 0.00128cm^2			

Following the standard relation,

$$J_{th} = J_0 \, exp \frac{T}{T_0} \qquad 5.1$$

Solving this equation for T_0, we get,

$$T_0 = \frac{\Delta T}{\Delta \, ln J_{th}} \qquad 5.2$$

As shown in Figure 5.5, $ln(J_{th})$ was plotted against absolute temperature T(K), and a linear fit was applied. The slope of the fitted line yields ($1/T_0$), from which the characteristic temperature (T_0) was extracted. This procedure provides the characteristic temperature T_0 = 109.17 ºC for standard cavity length (1600µm) by directly linking the temperature dependence of threshold to the exponential model.

5.5. Far field profile

The far-field intensity profiles of the 1600 µm cavity laser diode operated at 1000 mA, measured along the fast axis (red) and slow axis (blue) is shown in Figure 5.6. The fast axis exhibits a broad divergence with a full width at half maximum (FWHM) of approximately 53.3°, while the slow axis shows a much narrower divergence of about 9.0°. This anisotropic emission is a typical characteristic of edge-emitting semiconductor lasers, originating from the strong optical confinement in the vertical direction (fast axis)

and the weaker confinement along the lateral waveguide (slow axis) as already discussed in the section 3.2

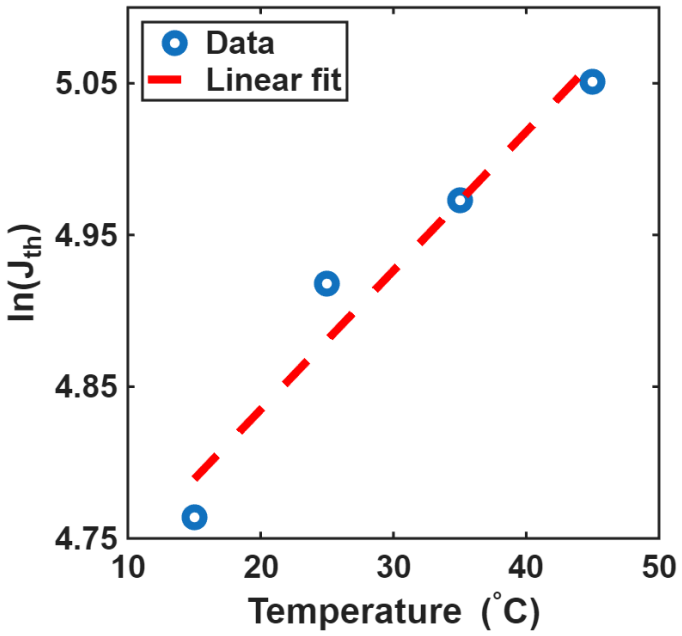

Figure 5.5 Threshold current density J_{th} versus temperature with linear fit; the inverse of the fit slope gives the characteristic temperature T_0.

5.6. Emission spectrum

The measured emission spectra for the 940-nm design device in Figure 5.7 show a systematic red shift of the lasing peak with increasing drive current i e λ≈935 nm at 500 mA, λ ≈940 nm at 1000 mA, and λ ≈947 nm at 2500 mA. This behavior is consistent with current-induced self-heating: as junction temperature rises, the semiconductor band gap narrows (Varshni dependence [24]), moving the material gain peak to longer wavelength, while the effective refractive index increases, lengthening the optical path and shifting the cavity modes to longer wavelengths. For GaAs-based lasers near 940 nm, a typical thermo-wavelength coefficient of ~0.25-0.35 nm K^{-1} can account for the observed drift [47].

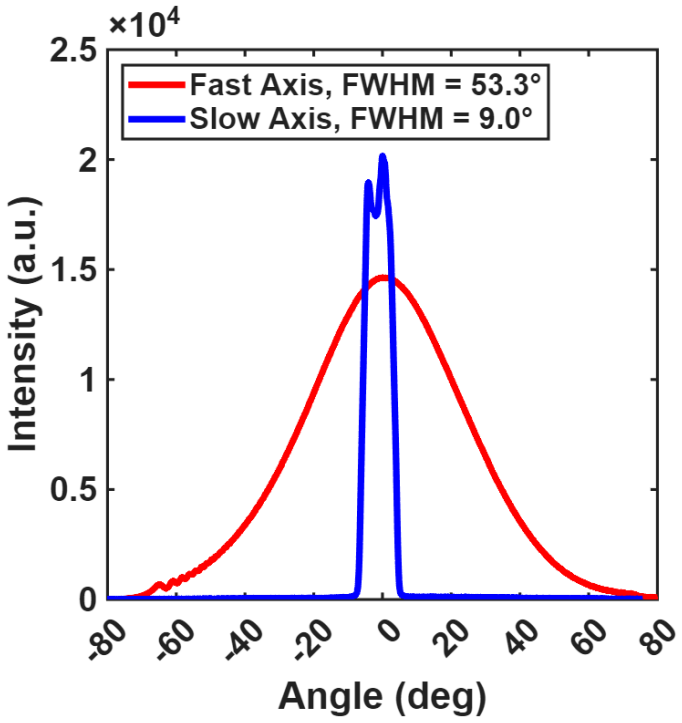

Figure 5.6 Far-field profiles of a 1600 μm GaAs laser diode at 1000 mA, showing broad fast-axis divergence (FWHM ≈ 53.3°) and narrow slow-axis divergence (FWHM ≈ 9.0°) due to anisotropic optical confinement.

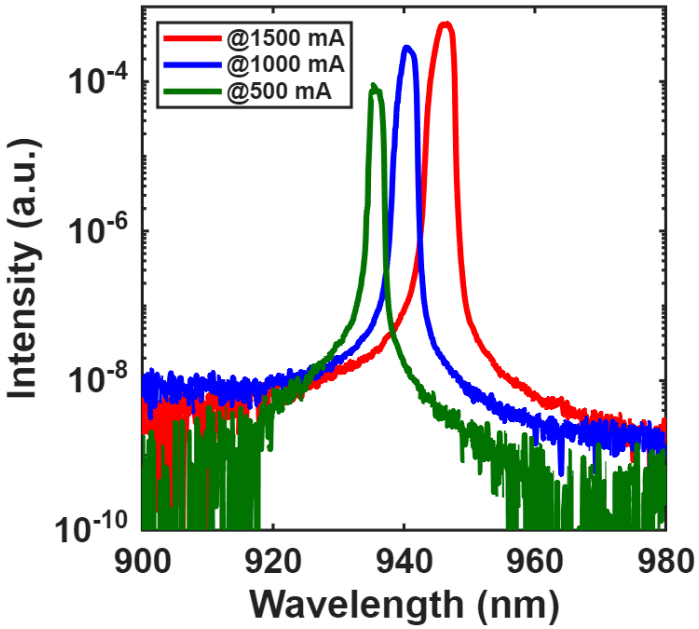

Figure 5.7 Room-temperature emission spectra of the 940-nm design device at different currents. The lasing peak redshifts with increasing current due to self-heating.

5.7. Power stability check

The device was operated in CW at a fixed injection current of 250 mA, i.e., with a modest margin above the measured threshold of 170 mA. This operating point deliberately emphasizes sensitivity to optical loss and modal dynamics while avoiding excessive self-heating. The resulting 24-hour power record Figure 5.8 serves as a functional stability probe: at constant current, any evolution in output directly reflects changes in internal optical loss and recombination dynamics rather than electrical drive.

The trace is broadly stable, with slow variations that are characteristic of electro-thermal and modal effects in double-heterostructure edge emitters. Because the drive current is held constant and the I-V response in this range is featureless, fluctuations in output power are not electrical in origin. Instead, they arise from small changes in refractive index (carrier and thermo-optic) and carrier distributions that subtly alter the modal overlap with lossy regions, manifesting as slight adjustments of external differential efficiency. This interpretation is consistent with the earlier L-I analysis in which a kink was attributed to integrating sphere range change.

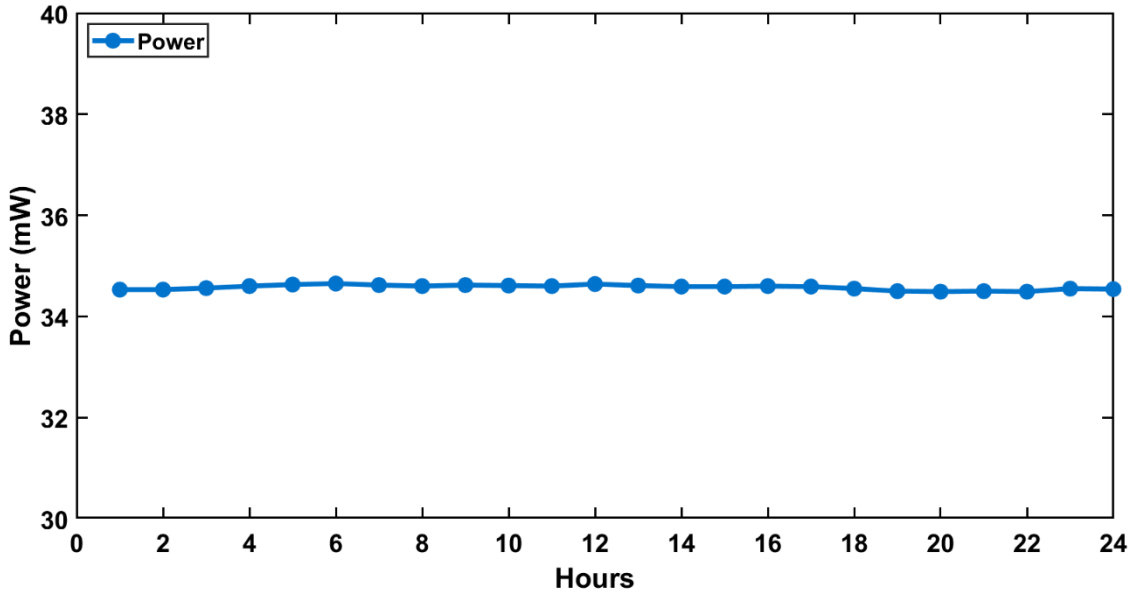

Figure 5.8 24-hour CW power stability at constant current (250 mA; I>Ith=170 mA). Slow variations in output reflect electro-thermal/modal dynamics, while the overall stability is limited predominantly by non-radiative recombination

6. Conclusion

This thesis aimed to advance the understanding and development of GaAs-based 940 nm edge-emitting laser diodes through simulation, fabrication, and experimental characterization.

The simulation phase involved defining the epitaxial structure in the HAROLD laser simulator and analyzing fundamental properties such as optical mode confinement, refractive-index profile, and equilibrium and biased band diagrams. The simulated L-I characteristics predicted a threshold current near 100 mA and a maximum optical output power of approximately 1.1 W. Power-balance analysis showed that a non-negligible fraction of the input power was dissipated through non-radiative recombination and thermal losses, offering insight into the expected device performance after fabrication.

Guided by these simulations, two epitaxial wafers were grown with different waveguide compositions: a 25% Al design and a 12% Al design. Oxide-stripe lasers were fabricated from both wafers and subsequently characterized. The measured threshold currents were approximately 170 mA for the 25% Al device and 270 mA for the 12% Al device, with series resistances of ~0.33–0.35 Ω. Corresponding electrical input powers were 180 mW and 273 mW, respectively. Spectral measurements confirmed lasing near 940 nm at low injection, in good agreement with the targeted epitaxial design and simulated emission wavelength.

Internal quantum efficiency and internal loss parameters were determined to be. To evaluate reliability, the 25% Al device was operated slightly above threshold for nearly a day. The output power remained stable at approximately 34.5 mW, indicating no significant degradation or Al-oxide-related instability under the tested conditions.

Overall, the results of this thesis provide a methodology for designing and assessing GaAs-based 940 nm stripe-oxide edge-emitting lasers, demonstrating good agreement between simulation and experiment across threshold behavior, emission wavelength, and optical stability. The study highlights the effectiveness of combining numerical modeling with systematic fabrication and characterization to guide the development of oxide-confined laser diodes.

Future work

Future work may focus on improving the optical performance and long-term stability of the 940 nm GaAs edge-emitting laser structures investigated in this thesis. Since the

oxide-stripe devices fabricated here were primarily used to evaluate the underlying epitaxial wafers quality, a recommended next step would be to implement optimized HR facet coating on fact just after dicing the chips to reduce mirror losses, enhance slope efficiency, and enable a more accurate assessment of the intrinsic gain characteristics of the epitaxial design. Furthermore, such improvements would provide a more comprehensive understanding of device performance and support the transition from preliminary epi-wafer testing toward better quality laser diodes.

Reference

[1] G. Roelkens *et al.*, “Silicon-Based Photonic Integration Beyond the Telecommunication Wavelength Range,” *IEEE J. Sel. Top. Quantum Electron.*, vol. 20, no. 4, pp. 394–404, July 2014, doi: 10.1109/JSTQE.2013.2294460.

[2] T. Jiang, H. Zhou, and Y. Yang, “Research on photonic communication technology and its prospects for defense applications,” in *Advanced Fiber Laser Conference (AFL2023)*, SPIE, Mar. 2024, pp. 1041–1046. doi: 10.1117/12.3023559.

[3] K. D. Vos, I. Bartolozzi, E. Schacht, P. Bienstman, and R. Baets, “Silicon-on-Insulator microring resonator for sensitive and label-free biosensing,” *Opt. Express*, vol. 15, no. 12, pp. 7610–7615, June 2007, doi: 10.1364/OE.15.007610.

[4] X. Zhou, A. Shen, S. Hu, W. Ni, X. Wang, and E. Hossain, “Towards Quantum-Native Communication Systems: State-of-the-Art, Trends, and Challenges,” *IEEE Commun. Surv. Tutor.*, pp. 1–1, 2025, doi: 10.1109/COMST.2025.3575842.

[5] J. Wang, F. Sciarrino, A. Laing, and M. G. Thompson, “Integrated photonic quantum technologies,” *Nat. Photonics*, vol. 14, no. 5, pp. 273–284, May 2020, doi: 10.1038/s41566-019-0532-1.

[6] Y. Lin *et al.*, “Monolithically integrated, broadband, high-efficiency silicon nitride-on-silicon waveguide photodetectors in a visible-light integrated photonics platform,” *Nat. Commun.*, vol. 13, no. 1, p. 6362, Oct. 2022, doi: 10.1038/s41467-022-34100-3.

[7] J. Zhou *et al.*, “High-Performance Thin-Film Lithium Niobate Mach–Zehnder Modulator on 8-inch Silicon Substrates,” *IEEE Photonics Technol. Lett.*, vol. 36, no. 17, pp. 1077–1080, Sept. 2024, doi: 10.1109/LPT.2024.3434542.

[8] C. Joshi, A. Farsi, S. Clemmen, S. Ramelow, and A. L. Gaeta, “Frequency multiplexing for quasi-deterministic heralded single-photon sources,” *Nat. Commun.*, vol. 9, no. 1, p. 847, Feb. 2018, doi: 10.1038/s41467-018-03254-4.

[9] D. Llewellyn *et al.*, “Chip-to-chip quantum teleportation and multi-photon entanglement in silicon,” *Nat. Phys.*, vol. 16, no. 2, pp. 148–153, Feb. 2020, doi: 10.1038/s41567-019-0727-x.

[10] P. Sibson *et al.*, “Chip-based quantum key distribution,” *Nat. Commun.*, vol. 8, no. 1, p. 13984, Feb. 2017, doi: 10.1038/ncomms13984.

[11] T. Gao, M. von Helversen, C. Antón-Solanas, C. Schneider, and T. Heindel, “Atomically-thin single-photon sources for quantum communication,” *Npj 2D Mater. Appl.*, vol. 7, no. 1, p. 4, Jan. 2023, doi: 10.1038/s41699-023-00366-4.

[12] R. Alléaume *et al.*, “Experimental open-air quantum key distribution with a single-photon source,” *New J. Phys.*, vol. 6, no. 1, p. 92, July 2004, doi: 10.1088/1367-2630/6/1/092.

[13] W. G. Fisher, E. A. Wachter, M. Armas, and C. Seaton, “Titanium:Sapphire Laser as an Excitation Source in Two-Photon Spectroscopy,” *Appl. Spectrosc.*, vol. 51, no. 2, pp. 218–226, Feb. 1997.

[14] M. L. Davenport, S. Liu, and J. E. Bowers, “Integrated heterogeneous silicon/III–V mode-locked lasers,” *Photonics Res.*, vol. 6, no. 5, pp. 468–478, May 2018, doi: 10.1364/PRJ.6.000468.

[15] M. T. Kelemen *et al.*, “High-power high-brightness ridge-waveguide tapered diode lasers at 940 nm,” in *Test and Measurement Applications of Optoelectronic Devices*, SPIE, Apr. 2002, pp. 75–81. doi: 10.1117/12.462644.

[16] Z. Jankiewicz and A. Zajac, “Medical applications of laser-emitting radiation within the range 1000 to 3000 nm,” in *Laser Technology IV: Applications in Medicine*, SPIE, Mar. 1995, pp. 20–30. doi: 10.1117/12.203337.

[17] M. D’Hondt *et al.*, “High quality InGaAs/AlGaAs lasers grown on Ge substrates,” *J. Cryst. Growth*, vol. 195, no. 1, pp. 655–659, Dec. 1998, doi: 10.1016/S0022-0248(98)00652-6.

[18] R. A. Salii, A. V. Malevskaya, D. A. Malevskii, S. A. Mintairov, A. M. Nadtochiy, and N. A. Kalyuzhnyy, “Light-Emitting AlGaAs/GaAs Diodes Based on InGaAs Strain-Compensated Quantum Wells with Minimized Internal Losses Caused by 940-nm Radiation Absorption,” *Crystallogr. Rep.*, vol. 69, no. 4, pp. 620–628, Aug. 2024, doi: 10.1134/S1063774524601485.

[19] J. Singh, *Electronic and Optoelectronic Properties of Semiconductor Structures*. Cambridge: Cambridge University Press, 2003. doi: 10.1017/CBO9780511805745.

[20] B. G. Streetman and S. Banerjee, *Solid state electronic devices*, Seventh edition. Boston: Pearson, 2015.

[21] L. A. Coldren, S. W. Corzine, and M. L. Mashanovitch, *Diode Lasers and Photonic Integrated Circuits*, 2nd ed., vol. 218. in Wiley series in microwave and optical engineering, vol. 218. Newark: Wiley, 2012.

[22] G. P. Agrawal and N. K. Dutta, *Semiconductor Lasers*. Boston, MA: Springer US, 1993. doi: 10.1007/978-1-4613-0481-4.

[23] A. Tomita and A. Suzuki, “Carrier-induced lasing wavelength shift for quantum well laser diodes,” *IEEE J. Quantum Electron.*, vol. 23, no. 7, pp. 1155–1159, July 1987, doi: 10.1109/JQE.1987.1073481.

[24] J. Piprek, *Semiconductor Optoelectronic Devices: Introduction to Physics and Simulation*. Academic Press, 2003.

[25] M. Loeser and B. Witzigmann, “Multidimensional Electro-Opto-Thermal Modeling of Broad-Band Optical Devices,” *IEEE J. Quantum Electron.*, vol. 44, no. 6, pp. 505–514, June 2008, doi: 10.1109/JQE.2008.917786.

[26] A. Sugimura, “Band-to-band Auger effect in GaSb and InAs lasers,” *J. Appl. Phys.*, vol. 51, no. 8, pp. 4405–4411, Aug. 1980, doi: 10.1063/1.328261.

[27] N. K. Dutta and R. J. Nelson, “The case for Auger recombination in In1−xGaxAsyP1−y,” *J. Appl. Phys.*, vol. 53, no. 1, pp. 74–92, Jan. 1982, doi: 10.1063/1.329942.

[28] J. R. Meyer *et al.*, “Auger coefficients in type-II InAs/Ga1−xInxSb quantum wells,” *Appl. Phys. Lett.*, vol. 73, no. 20, pp. 2857–2859, Nov. 1998, doi: 10.1063/1.122609.

[29] H. P. Hjalmarson and S. R. Kurtz, “Electron Auger processes in mid-infrared InAsSb/InGaAs heterostructures,” *Appl. Phys. Lett.*, vol. 69, no. 7, pp. 949–951, Aug. 1996, doi: 10.1063/1.117091.

[30] A. Sugimura, “Band-to-band auger effect in long wavelength multinary III-V alloy semiconductor lasers,” *IEEE J. Quantum Electron.*, vol. 18, no. 3, pp. 352–363, Mar. 1982, doi: 10.1109/JQE.1982.1071543.

[31] L. Shterengas, G. L. Belenky, J. G. Kim, and R. U. Martinelli, “Design of high-power room-temperature continuous-wave GaSb-based type-I quantum-well lasers with λ

> 2.5 μm," *Semicond. Sci. Technol.*, vol. 19, no. 5, p. 655, Feb. 2004, doi: 10.1088/0268-1242/19/5/016.

[32] N. J. Butt, R. A. Roberts, and S. S. Patnaik, "Laser diode optical output dependence on junction temperature for high-power laser systems," *Opt. Laser Technol.*, vol. 125, p. 106019, May 2020, doi: 10.1016/j.optlastec.2019.106019.

[33] T. Newell, X. Wu, A. L. Gray, S. Dorato, H. Lee, and L. F. Lester, "The effect of increased valence band offset on the operation of 2 μm GaInAsSb-AlGaAsSb lasers," *IEEE Photonics Technol. Lett.*, vol. 11, no. 1, pp. 30–32, Jan. 1999, doi: 10.1109/68.736380.

[34] R. People and J. C. Bean, "Calculation of critical layer thickness versus lattice mismatch for GexSi1 - x/Si strained-layer heterostructures," *Appl. Phys. Lett.*, vol. 47, pp. 322–324, Aug. 1985, doi: 10.1063/1.96206.

[35] S. C. Jain, J. M. McGregor, and D. J. Roulston, "Band-gap narrowing in novel III-V semiconductors," *J. Appl. Phys.*, vol. 68, no. 7, pp. 3747–3749, Oct. 1990, doi: 10.1063/1.346291.

[36] J. J. Coleman, "Strained-layer InGaAs quantum-well heterostructure lasers," *IEEE J. Sel. Top. Quantum Electron.*, vol. 6, no. 6, pp. 1008–1013, Nov. 2000, doi: 10.1109/2944.902149.

[37] G. H. B. Thompson, *Physics of semiconductor laser devices*. 1980. Accessed: Dec. 15, 2025. [Online]. Available: https://ui.adsabs.harvard.edu/abs/1980wi...book.....T

[38] W. T. Tsang, "The effects of lateral current spreading, carrier out-diffusion, and optical mode losses on the threshold current density of GaAs-AlχGa1-χAs stripe-geometry DH lasers," *J. Appl. Phys.*, vol. 49, pp. 1031–1044, Mar. 1978, doi: 10.1063/1.325040.

[39] P. W. Epperlein, *Semiconductor Laser Engineering, Reliability and Diagnostics: A Practical Approach to High Power and Single Mode Devices*. John Wiley & Sons, 2013.

[40] D. Liang, J. Wang, and D. C. Hall, "Nonselective oxidation of GaAs-based III-V compound semiconductor heterostructures for in-plane semiconductor lasers," in *Novel In-Plane Semiconductor Lasers VI*, SPIE, Feb. 2007, pp. 190–203. doi: 10.1117/12.701648.

[41] A. G. Baca, C. I. H. Ashby, and I. of E. Engineers, *Fabrication of GaAs Devices*. IET, 2005.

[42] J. Shul and S. L. Pearton (eds), "Handbook of Advanced Plasma Processing Techniques," *Plasma Phys. Control. Fusion*, vol. 43, no. 3, p. 372, Mar. 2001, doi: 10.1088/0741-3335/43/3/703.

[43] N. Vodjdani and P. Parrens, "Reactive ion etching of GaAs with high aspect ratios with Cl2–CH4–H2–Ar mixtures," *J. Vac. Sci. Technol. B Microelectron. Process. Phenom.*, vol. 5, no. 6, pp. 1591–1598, Nov. 1987, doi: 10.1116/1.583634.

[44] M. A. Herman and H. Sitter, *Molecular Beam Epitaxy: Fundamentals and Current Status*. Springer Science & Business Media, 2012.

[45] E. Mobini, D. H. G. Espinosa, K. Vyas, and K. Dolgaleva, "AlGaAs Nonlinear Integrated Photonics," *Micromachines*, vol. 13, no. 7, p. 991, July 2022, doi: 10.3390/mi13070991.

[46] R. T. Lynch Jr., M. B. Small, and R. Y. Hung, "Effect of cavity length on stripe-geometry DH laser output linearity," *Appl. Phys. Lett.*, vol. 34, no. 4, pp. 297–299, Feb. 1979, doi: 10.1063/1.90766.

[47] Y. Liao *et al.*, “An Experimental Study on the Temperature Characteristic of a 940 nm Semiconductor Laser Diode,” *Opt. Photonics J.*, vol. 6, no. 8, pp. 75–82, Aug. 2016, doi: 10.4236/opj.2016.68B013.